

Generative Spatio-temporal GraphNet for Transonic Wing Pressure Distribution Forecasting

Gabriele Immordino^{a,1,*}, Andrea Vaiuso^{1,2}, Andrea Da Ronch^{a,3}, Marcello Righi^{1,4}

^a*Faculty of Engineering and Physical Sciences, University of Southampton, Southampton, United Kingdom*

^b*School of Engineering, Zurich University of Applied Sciences ZHAW, Winterthur, Switzerland*

Abstract

This study presents a framework for predicting unsteady transonic wing pressure distributions, integrating an autoencoder architecture with graph convolutional networks and graph-based temporal layers to model time dependencies. The framework compresses high-dimensional pressure distribution data into a lower-dimensional latent space using an autoencoder, ensuring efficient data representation while preserving essential features. Within this latent space, graph-based temporal layers are employed to predict future wing pressures based on past data, effectively capturing temporal dependencies and improving predictive accuracy. This combined approach leverages the strengths of autoencoders for dimensionality reduction, graph convolutional networks for handling unstructured grid data, and temporal layers for modeling time-based sequences. The effectiveness of the proposed framework is validated through its application to the Benchmark Super Critical Wing test case, achieving accuracy comparable to computational fluid dynamics, while significantly reducing prediction time. This framework offers a scalable, computationally efficient solution for the aerodynamic analysis of unsteady phenomena.

*Corresponding Author

Email address: G.Immordino@soton.ac.uk (Gabriele Immordino)

¹Ph.D. Student

²Research Associate

³Professor, AIAA Senior Member

⁴Professor, AIAA Member, Lecturer at Federal Institute of Technology Zurich ETHZ

Nomenclature

Acronyms

<i>AE</i>	=	autoencoder
<i>CFD</i>	=	computational fluid dynamics
<i>GCN</i>	=	graph convolutional network
<i>GNN</i>	=	graph neural network
<i>GRU</i>	=	gated recurrent unit
<i>GST</i>	=	generative spatio-temporal
<i>LSTM</i>	=	long short-term memory
<i>ML</i>	=	machine learning
<i>MAE</i>	=	mean absolute error
<i>MAPE</i>	=	mean absolute percentage error
<i>MWLS</i>	=	moving weighted least squares
<i>RMSE</i>	=	root mean square error
<i>ROM</i>	=	reduced-order model
<i>STGCN</i>	=	spatio-temporal GCN

Symbols

C_L	=	lift coefficient
C_M	=	pitching moment coefficient
C_P	=	pressure coefficient
M	=	Mach number
θ	=	pitch angle, rad
$\dot{\theta}$	=	pitch rate, rad/s
$\ddot{\theta}$	=	pitch acceleration, rad/s ²
ξ	=	plunge, m
$\dot{\xi}$	=	plunge rate, m/s
$\ddot{\xi}$	=	plunge acceleration, m/s ²

1. Introduction

The complexity of aerodynamic analysis poses a significant challenge across various engineering applications. Accurately predicting challenging physical phenomena involves capturing detailed variations that arise from the complex interaction of multiple forces. Traditional computational fluid dynamics (CFD) methods are effective in many scenarios, but often require substantial computational resources and may struggle with accurately representing dynamic and unsteady phenomena under specific flow conditions [1, 2]. These limitations highlight the need for more efficient and robust approaches.

Recent advancements in machine learning (ML) offer promising solutions for these challenges. Initially, deep neural networks were applied to capture complex patterns in fluid dynamics [3, 4, 5, 6]. However, aerospace engineering problems often rely on non-homogeneous and unstructured grids modeling, which necessitate more advanced ML architectures that can handle this complex data structures.

Geometric deep learning, introduced around 2017 [7], utilizes graph neural networks (GNNs) for graph-structured data [8, 9]. GNNs excel in capturing relationships and dependencies within graph nodes, making them ideal for tasks involving topological information [10, 11, 12]. Graph Convolutional Networks (GCNs), a specific type of GNN, leverage convolution operations on graphs to enhance their capability

to process graph-structured data [13]. GCNs are particularly promising in aerospace engineering, as they can handle data with spatial structures and are suitable for modeling complex aerodynamic geometries [14, 15, 16, 17, 18]. In fact, while Convolutional Neural Networks (CNNs) perform well on regular grid data like images and texts, GCNs are better suited for irregular domains, such as mesh grids, by applying convolution operations directly on graphs [13]. Indeed, GCNs can directly input raw 3D model mesh data without pre-computation or feature extraction, enhancing predictive capabilities without bias or information loss [10].

Another important challenge concerns the high dimensionality of model input data. As with CNN architectures for image recognition tasks, deep and complex architectures struggle with propagating information over a large number of features. CFD simulations typically involve the use of fine meshes, consisting of a significantly large number of points, increasing both complexity and computational requirements. To manage this, careful data compression is needed to retain only the essential features without losing critical information. Previous studies have demonstrated that dimensionality reduction can be effectively achieved using an autoencoder (AE) architecture [19, 18, 20, 21]. AEs, through their encoding and decoding processes, can learn a compact and efficient representation of the data, ensuring that critical information is preserved while reducing the computational burden [22, 23].

Building on our previous study [24], which focused on steady-state problems, we now extend our methodology to address unsteady phenomena. Predicting time-varying pressure distributions relies primarily on capturing temporal dependencies within the data. Recurrent Neural Networks (RNNs), with their ability to track evolving patterns through a hidden state, are particularly well-suited for this task. Their effectiveness in modeling unsteady behaviors and dynamic responses makes them an ideal choice for forecasting time series in aerodynamic applications [25, 26]. However, RNNs often struggle with long-term dependencies due to challenges like vanishing gradients [27]. To address these limitations, Long Short-Term Memory (LSTM) networks and Gated Recurrent Units (GRUs), both RNN variants, have been developed. LSTMs introduce gates that control the flow of information, making them more effective at learning long-term dependencies [25]. GRUs offer a simpler structure than LSTMs, using fewer gates while still managing to capture long-term dependencies, often with faster training times [26]. LSTMs have been extensively applied in aerodynamic modeling, such as predicting the dynamic response of aeroelastic systems and turbulence [28, 29], while GRUs have also proven effective for similar tasks [30, 31]. More recently, attention mechanisms have revolutionized time series forecasting by enabling models to focus on the most relevant parts of the input sequence [32, 33]. This capability leads to more accurate and robust predictions,

as demonstrated for instance by improvements in maintenance scheduling through estimating icing probabilities on wind turbine blades [34], stable long-term fluid dynamics predictions using transformer-style temporal attention [35], and enhanced design and control of hypersonic vehicles by capturing spatiotemporal turbulence characteristics [36]. Attention mechanisms enable models to weigh the importance of different time steps dynamically, thereby improving the ability to model complex temporal patterns. Similarly, Spatio-Temporal Graph Convolution Networks (STGCNs) have shown strong performance in modeling such patterns by processing entire sequences in parallel and applying filters across the time dimension, capturing both short- and long-term dependencies efficiently [37].

To fully harness the potential of these temporal modeling techniques, it is important to recognize that each approach offers distinct benefits depending on the nature of the data and the specific application. With this in mind, our methodology investigates and evaluates several temporal layers—LSTMs, GRUs, attention mechanisms, and STGCNs—to effectively capture the temporal dependencies in our case study. By integrating graph convolutional networks with AEs and temporal layers, our proposed approach leverages the strengths of each method to enhance the prediction of unsteady surface pressure distributions over a transonic wing. This integrated framework not only handles the unstructured grids typical in aerodynamic data through GCNs but also ensures efficient dimensionality reduction through AEs. By comparing different temporal approaches, we aim to provide a comprehensive and scalable solution for complex aerodynamic analyses, delivering more accurate and computationally efficient predictions for unsteady phenomena.

The structure of the paper is as follows: Section 2 details the implemented methodology, providing a comprehensive explanation of the architecture and its components. Section 3 describes the test case used to validate the model, focusing on its aerodynamic challenges. Section 4 presents the results, comparing the performance of different architectures designed to address temporal challenges, while evaluating the impact of various temporal layers. Finally, Section 5 summarizes the conclusions drawn from the study and suggests potential future directions for improving the model accuracy and scalability in different aerodynamic scenarios.

2. Methodology

This section outlines the methodology used in developing the model. It begins with an overview of the Generative Spatio-Temporal (GST) GraphNet framework, then provides an in-depth description of each component of the model.

2.1. Generative Spatio-Temporal GraphNet

The proposed GST GraphNet framework integrates a GCN-based AE architecture with a temporal prediction layer to effectively model and forecast wing pressure distributions for subsequent timesteps. The encoding and decoding modules operate with graph nodes based on the pressure-gradient distribution values across the wing surface, performing pooling and unpooling operations on the input, respectively. Initially, a pre-trained AE is used to compress the pressure distribution data into a lower-dimensional representation, preserving fundamental features while reducing computational complexity. This pre-training step reduces the full model training time and computational costs, enhancing the overall efficiency of the prediction process. After the pooling operation, the reduced-space representation is passed through a temporal prediction layer. This layer is designed to capture the temporal dependencies in the data and forecast wing pressure from a series of previous timesteps to a future one. To account for the complexities caused by shock waves and boundary layer separation, which affect force and moment calculations, a penalty term for the pitching moment coefficient C_{M_y} is added to the Mean Absolute Error (MAE) loss function. This addition is represented as $Loss = MAE + \lambda \cdot C_{M_y}$, with $\lambda = 0.01$ for dimensional consistency. The combination of AE, GCN layers, and temporal modeling enables the framework to provide precise and reliable pressure predictions, which are crucial for analyzing aerodynamic performance.

A visual overview of the model architecture is presented in Figure 1. The model input features include data from the n previous timesteps ($t - 1, \dots, t - n$): spatial coordinates (x, y, z); pitch ($\theta_{t-n}, \dot{\theta}_{t-n}, \ddot{\theta}_{t-n}$); plunge ($\xi_{t-n}, \dot{\xi}_{t-n}$); and pressure coefficient ($C_{P_{t-n}}$), with $n = 3$. Finally, the output of the model is represented by the pressure coefficient (C_{P_t}) at the current timestep t . The choice of this sequence length ensures that the model has access to sufficient temporal context to capture the evolution of unsteady aerodynamic features, such as flow separation and shock dynamics, while avoiding the inclusion of redundant or excessive data, which would increase computational complexity without significantly improving accuracy.

Building on this, we developed two different types of architecture: a feedforward model and an autoregressive-moving-average model with exogenous inputs (ARMAX) model. In the case of the feedforward model, the inputs consist solely of the coordinates of the wing surface and the prescribed motion at n previous timesteps casted on each graph node (using only Module B in Figure 1). This model does not incorporate any past predicted pressures into its input, relying purely on the historical spatial and motion data of the wing to make its predictions. Conversely, the ARMAX model includes additional information in its input by integrating the pressures predicted at prior timesteps (utilizing both Module A and Module B in

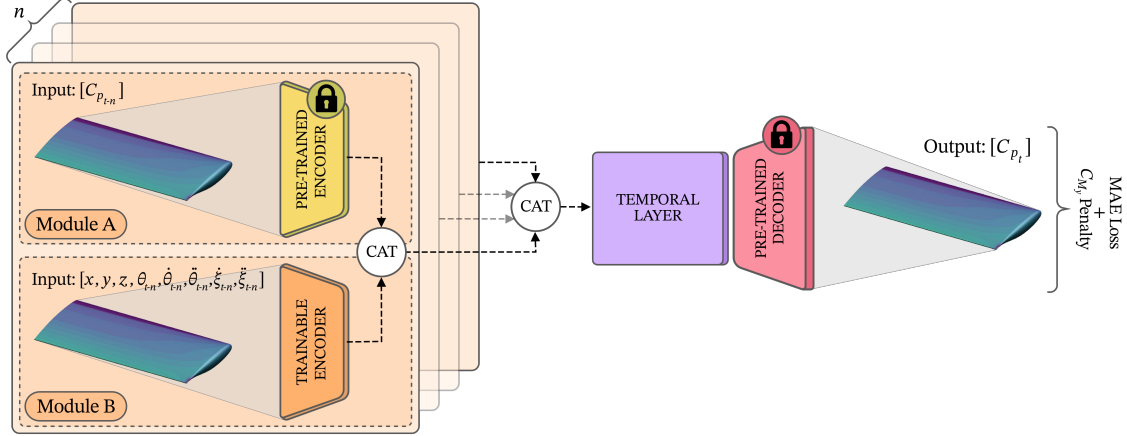


Figure 1: Overview of the GST GraphNet architecture for predicting wing pressure distributions. Module A represents the autoregressive component, incorporating previously predicted C_P values, while Module B processes spatial coordinates and motion data from previous timesteps.

Figure 1). This autoregressive component allows the ARMAX model to potentially capture more complex temporal dependencies by considering the history of its own predictions, aiming to enhance the accuracy of the pressure forecasts. Implementing both models serves to evaluate the trade-offs between simplicity and predictive depth: while the feedforward model offers a simpler, stable approach less prone to error accumulation, the ARMAX model is designed to capture complex temporal dependencies and unsteady behaviors, potentially enhancing accuracy under dynamic conditions.

To limit error accumulation in the time-marching scheme, we employed a Back-Propagation Through Time (BPTT) algorithm [27] for the total loss calculation, dividing the dataset into mini-sequences. The model processes each sequence consecutively, accumulating error over time. After processing each sequence, the loss function is applied to update the model parameters through backpropagation. A sequence length of three was chosen based on its performance, yielding the best results.

2.1.1. Graph Representation

A graph G is defined by a set of nodes N and edges E , where each edge (i, j) represents a directed link from node i to node j . Self-loops occur when $(i, i) \in E$. These connections are represented by an adjacency matrix \mathbf{A} , where $\mathbf{A}_{ij} = 1$ if $(i, j) \in E$, and 0 otherwise. Costs for edges can be included by replacing 1 with the cost and using ∞ for absent connections. A path $p(i \rightarrow j)$ is a series of steps from i

to j , where each step $(h, k) \in E$. A graph is acyclic if no path returns to a starting node, otherwise, it is cyclic.

In our case, the mesh can be represented as a cyclic graph G , where each grid point i serves as a node. Each node carries features such as spatial coordinates (x, y, z) , pitch $(\theta, \dot{\theta}, \ddot{\theta})$, plunge $(\xi, \dot{\xi})$, and the pressure coefficient C_P from the previous n timesteps. We call node features y_i , while edge weights e_{ij} .

Graph connectivity is represented by the adjacency matrix \mathbf{A} , where each weight e_{ij} is the Euclidean distance between grid points i and j : $e_{ij} = \|\mathbf{x}_i - \mathbf{x}_j\|_2$. To normalize the weights to $(0, 1]$ and include self-loops ($e_{ii} = 1$), the adjacency matrix is augmented: $\tilde{\mathbf{A}} = \mathbf{A} + \mathbf{I}$. Since edges are bidirectional ($e_{ij} = e_{ji}$), $\tilde{\mathbf{A}}$ is symmetric.

Due to the graph sparsity, the adjacency matrix is stored in a memory-efficient Coordinate List (COO) format, where the edge-index matrix contains pairs of node indices, and the edge-weight matrix stores the corresponding weights, with n_e being the number of edges.

2.1.2. Graph Convolutional Networks

GCNs are a particular type of ML algorithms that are based on graph theory. GCNs extract features from graphs by aggregating information from neighboring nodes using a graph convolutional operator. This operator, originally introduced by Duvenaud et al. in 2015 for molecular fingerprints [38], was later extended by Kipf et al. in 2016 [13] and is now implemented in PyTorch-Geometric library [39]. GCNs effectively generate node embeddings that capture structural information, making them ideal for tasks requiring an understanding of relationships between nodes.

The GCN operator follows the layer-wise propagation rule that is defined by the equation:

$$H^{(l+1)} = \sigma(\tilde{\mathbf{D}}^{-\frac{1}{2}} \tilde{\mathbf{A}} \tilde{\mathbf{D}}^{-\frac{1}{2}} H^{(l)} W^{(l)}) \quad (1)$$

Here, $H^{(l)}$ and $H^{(l+1)}$ are the node feature matrices at layers l and $l+1$, $\tilde{\mathbf{A}}$ is the adjacency matrix with self-loops, $\tilde{\mathbf{D}}$ is the degree matrix calculated on $\tilde{\mathbf{A}}$, $W^{(l)}$ is the matrix of trainable weights, and σ is the activation function. This rule propagates information from a node to its neighbors, allowing nodes to gather information from larger neighborhoods as layers are stacked. Equation 1 is a first-order approximation of trainable localized spectral filters g_θ on graphs [13].

A spectral convolution $g_\theta * x$ of an input graph \tilde{x} with a filter g_θ in the Fourier domain is defined as:

$$g_\theta * x = \mathbf{U} g_\theta \mathbf{U}^T x \quad (2)$$

where \mathbf{U} contains the eigenvectors of the graph Laplacian, \mathbf{L} . By approximating the spectral filter g_θ using Chebyshev polynomials [40], GCNs perform efficient localized filtering on graph data. This approximation simplifies the convolution process, making it feasible for large-scale graphs while preserving the ability to extract meaningful node features.

2.2. Temporal Layers

In our framework, we explored various layers for temporal modeling: GRUs, LSTMs, attention mechanisms, and STGCN layers. Each method offers a distinct way to capture temporal dependencies, with varying level of complexity and performance suited to different contexts. In this section, we provide a brief overview of these methods, highlighting their key features and how they are integrated into our model. This comparison helps evaluate their effectiveness in handling temporal sequences.

Gated Recurrent Unit

The combination of GCNs with GRU [26] offers several key advantages when dealing with spatio-temporal data. GRUs are widely used and well-suited for modeling temporal dependencies, but they can not directly used with non-Cartesian domains like graphs, where spatial relationships are irregular. By incorporating graph convolution operators on GRUs, it is possible to improve the generalization capability of the model by replacing traditional convolution with a graph convolution, which can handle arbitrary graph structures and effectively learn from unstructured data.

Based on the approach in [41] where recurrent networks for fixed grid-structured sequence are introduced, Seo et al. [42] proposed a Graph Convolutional Recurrent Network (GCRN) architecture for building a generalized GRU that works with unstructured sequence. To generalize the model to graphs, the 2D convolution is replaced by the graph convolution operator, here $*_g$, introduced in (2). In particular, GRU cell in GCRN is defined by:

$$\begin{aligned} z_t &= \sigma(W_{xz} *_g x_t + U_{hz} *_g h_{t-1} + b_z) \\ r_t &= \sigma(W_{xr} *_g x_t + U_{hr} *_g h_{t-1} + b_r) \\ \hat{h}_t &= \phi(W_{xh} *_g x_t + U_{hh} *_g (r_t \odot h_{t-1}) + b_h) \\ h_t &= (1 - z_t) \odot h_{t-1} + z_t \odot \hat{h}_t \end{aligned}$$

Here, $W_{xz} *_g x_t$ refers to the graph convolution operation of x_t with spectral filters which are functions of the graph Laplacian L parametrized by K Chebyshev coefficients. z_t is the update gate vector, r_t is the reset gate vector, \hat{h}_t is the candidate

activation vector, h_t is the hidden state at time step t , W and U are the trainable weight matrices for the input and hidden states, respectively, σ is the logistic sigmoid function, and ϕ is the hyperbolic tangent function (or other possible activation functions). The operator \odot denotes the Hadamard product, while b represents the biases.

Long Short-Term Memory

LSTM networks [25] are particularly useful when the data involves long-term dependencies, as they include memory units that can store information across multiple timesteps. This makes them potentially suitable to model unsteady aerodynamic flows where past behavior influences future forecasts over long periods of time. While both LSTM and GRU address the vanishing gradient problem and are designed to capture temporal relationships, LSTM includes additional memory structures that enable it to retain information over longer time periods, by sacrificing computational power and increasing the number of parameters. The implementation of a convolutional graph based LSTM follows a similar approach presented before with GRU [42], by creating a model that replaces the 2D convolution with the graph convolution operator $*_g$. In particular:

$$\begin{aligned} i_t &= \sigma(W_{xi} *_g x_t + W_{hi} *_g h_{t-1} + w_{ci} \odot c_{t-1} + b_i) \\ f_t &= \sigma(W_{xf} *_g x_t + W_{hf} *_g h_{t-1} + w_{cf} \odot c_{t-1} + b_f) \\ c_t &= f_t \odot c_{t-1} + i_t \odot \phi(W_{xc} *_g x_t + W_{hc} *_g h_{t-1} + b_c) \\ o_t &= \sigma(W_{xo} *_g x_t + W_{ho} *_g h_{t-1} + w_{co} \odot c_t + b_o) \\ h_t &= o_t \odot \phi(c_t) \end{aligned}$$

Where i_t is the input gate, f_t the forget gate, c_t the cell state, o_t the output gate and h_t the hidden state, which is the output of the LSTM at time step t . As before, σ is the logistic sigmoid function, ϕ is the hyperbolic tangent function, W represents the trainable weight matrix, and the support K of the graph convolutional kernels is defined by the Chebyshev coefficients. This extension of the standard LSTM architecture enables the model to learn temporal dependencies while also taking into account the spatial structure of the data.

Attention Mechanisms

Incorporating attention mechanisms allows for dynamically assigning importance to different time steps in a temporal sequence, which is especially useful in graph-based models where both complex spatial and temporal dependencies must be captured. Following the work of Bai et al. [37], attention mechanisms can be employed to re-weight the influence of hidden states of a GCRN across time, enabling the

model to focus on the most relevant time points for prediction, rather than treating each equally. The model was constructed by combining GCN and GRU to compute both the spatial and temporal domains of the graph, by using the graph convolution operator $*_g$ introduced before. In addition, the attention mechanism is used to compute a context vector that selectively weighs the hidden states of the GCRN.

First, for each time step, the hidden states of the GRU h_t are passed through an attention layer, where attention scores α_t are computed using a softmax function. These scores are then used to weigh the hidden states, resulting in the context vector C , which captures the global variation information.

In particular, given a series of hidden states calculated by the recurrent network for T time steps: $H = \{h_1, h_2, \dots, h_T\}$, the attention weights $\alpha_t, 1 < t < T$ are computed using a softmax function on the scores derived from a multilayer perceptron (MLP):

$$e_t = w^{(2)}(w^{(1)}H + b^{(1)}) + b^{(2)}, \quad \alpha_t = \frac{\exp(e_t)}{\sum_{i=1}^T \exp(e_i)}$$

where $w^{(1)}, w^{(2)}, b^{(1)}$, and $b^{(2)}$ are trainable weights and biases in the MLP. The context vector C is then calculated by the weighted sum and used for implementing the attention mechanism on the GCRN hidden states:

$$C = \sum_{t=1}^T \alpha_t h_t$$

By combining GCNs for spatial feature extraction with GRUs and attention mechanisms for temporal modeling, the model can capture both short-term and long-term dependencies in the data.

Spatio-temporal Graph Convolution

STGCN is introduced by Yu et al. [43] as a method to capture temporal dependencies in spatio-temporal data by applying convolutions across the time dimension. Unlike RNNs, which process inputs sequentially, temporal convolutions handle entire sequences at once, allowing for parallelization and faster computation. The temporal convolutional block consists of 1-D causal convolutions followed by a Gated Linear Unit (GLU) to introduce non-linearity and control the flow of information.

For each node in the graph G , the temporal convolution layer explores K_t neighboring elements along the time axis. This approach does not require padding, and as a result, the length of the sequence decreases by $K_t - 1$ at each layer. Given an input sequence $Y \in \mathbb{R}^{M \times C_i}$ with M time steps and C_i channels, the convolution kernel

$\Gamma \in \mathbb{R}^{K_t \times C_i \times 2C_o}$ maps the input to a single output element $[P \ Q] \in \mathbb{R}^{(M-K_t+1) \times (2C_o)}$. The GLU is then applied, splitting $[P \ Q]$ into two parts, and the output of the temporal convolution is given by:

$$\Gamma *_{\mathcal{T}} Y = P \odot \sigma(Q) \in \mathbb{R}^{(M-K_t+1) \times C_o},$$

where P and Q are the inputs of the GLU, \odot denotes the element-wise Hadamard product, and σ is the sigmoid function. The GLU selectively gates the information flow, determining which parts of the input sequence are relevant for capturing dynamic temporal dependencies. Stacking multiple layers of these temporal convolutions enables the model to capture both short- and long-term patterns effectively.

This approach can also be generalized to 3D tensors, where the same convolution kernel is applied to every node $Y_i \in \mathbb{R}^{M \times C_i}$ in the graph G , resulting in the operation $\Gamma *_{\mathcal{T}} Y$ with $Y \in \mathbb{R}^{M \times n \times C_i}$.

2.3. Dimensionality Reduction/Expansion Module

The dimensionality reduction and expansion process aims to simplify the computational load by eliminating redundant information and concentrating on key regions where nonlinear phenomena occur. This method is based on our previous work [24] and is visualized in Figure 2, which illustrates both the pooling (reduction) and unpooling (expansion) phases. These phases form the core of the encoding and decoding operations in the AE architecture.

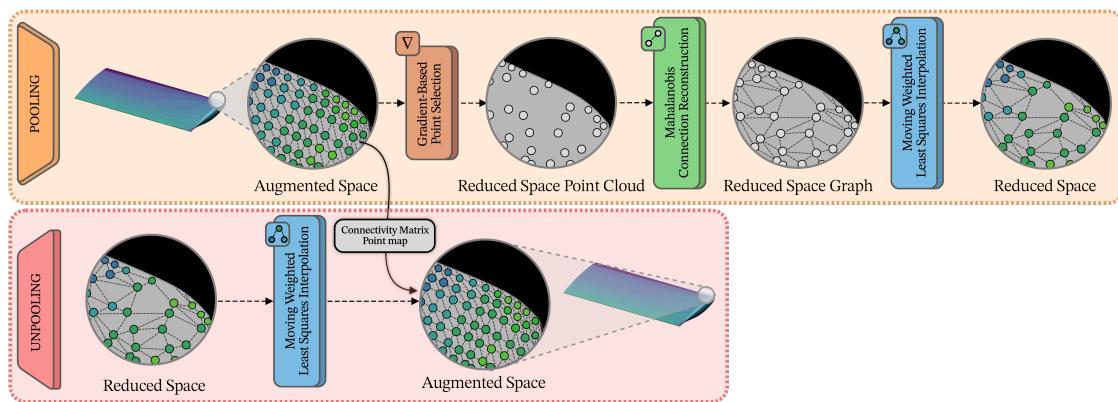


Figure 2: Diagram of the pooling and unpooling modules used in the AE for dimensionality reduction and reconstruction.

During the pooling phase, points are selected based on pressure gradients to create a reduced point cloud. This strategy ensures that key regions with high gradients

are retained, while areas with lower gradients are simplified. The pressure gradient at each node i is calculated assuming that pressure p varies linearly in all spatial directions, as described by:

$$p_i - p_0 = \Delta p_i = \Delta x_i p_x + \Delta y_i p_y + \Delta z_i p_z \quad (3)$$

Here, p_0 represents the pressure at a reference node, while Δx_i , Δy_i , and Δz_i are the spatial differences between neighboring nodes i . Using a least-squares method, the gradient at each node is determined. Nodes are then selected for the reduced space based on a probability function driven by gradient magnitudes:

$$p(i) = 1 + \frac{1 - e^{-2i/n}}{1 - e^{-2}}(p_1 - p_n) + p_1 \quad \text{for } i = 1, \dots, n \quad (4)$$

where i refers to the node index ordered by gradient values, n is the total number of nodes, and p_1 and p_n are the probabilities assigned to the highest and lowest gradient values, respectively.

To reconnect the reduced point cloud, Mahalanobis distance is used [44], which accounts for the spread and covariance of the point distribution. This method helps maintain accurate connectivity in the reduced graph, avoiding false connections caused by proximity errors under Euclidean distance [24]. The Mahalanobis distance between two points x and y is given by:

$$D_M(x, y) = \sqrt{(x - y)^T S^{-1} (x - y)} \quad (5)$$

where S is the covariance matrix of the original distribution.

Once the reduced graph is constructed, node values are interpolated using the Moving Weighted Least Squares (MWLS) method. The interpolation matrix $I_{S_s \rightarrow S_d}$ maps values from the source grid S_s to the destination grid S_d . The weights are assigned based on proximity, using the function $w(\mathbf{x}_i) = e^{-\|\mathbf{x} - \mathbf{x}_i\|^2}$. The final interpolated value at each node \mathbf{x}_j is then computed as:

$$u(\mathbf{x}_j) = \Phi(\mathbf{x}_j) \mathbf{y}_{S_s} \quad (6)$$

where:

$$\Phi(\mathbf{x}_j) = \mathbf{p}^T(\mathbf{x}_j) (\mathbf{P}^T \mathbf{W} \mathbf{P})^{-1} \mathbf{P}^T \mathbf{W} \quad (7)$$

In this equation, \mathbf{P} represents the design matrix for the source nodes, and \mathbf{W} is a diagonal matrix containing the Gaussian weights. The interpolation matrix $I_{S_s \rightarrow S_d}$ is used for pooling, and since it is not invertible, the inverse interpolation matrix $I_{S_d \rightarrow S_s}$ is computed separately for use in the unpooling phase (decoder).

For a detailed explanation of the entire encoding and decoding process, refer to the work of Immordino et al. [24].

2.4. Pre-trained Autoencoder

Our proposed framework leverages an AE architecture, pre-trained for subsequent integration into the complete model. The pre-training phase involved using C_P data as both input and output to the AE, ensuring the model accurately captures the essential features of the pressure distribution over the wing surface. The training dataset comprised the four signals detailed in Table 3.

To enhance the robustness of the AE, a data augmentation technique was employed. Specifically, the dataset was augmented by 30% through the addition of Gaussian noise with 10% standard deviation of the input data. This augmentation strategy was designed to improve the model ability to generalize and handle variability in the pressure distribution data. Skip connections were integrated before each encoding module to facilitate the direct flow of information across the network. These connections allow the model to bypass certain layers, enabling the retention of critical features and mitigating the risk of information loss during the encoding and decoding processes. The network architecture has been optimized using a Bayesian optimization strategy, following the same approach of our previous work [24]. A schematic of the pre-trained AE architecture is shown in Figure 3.

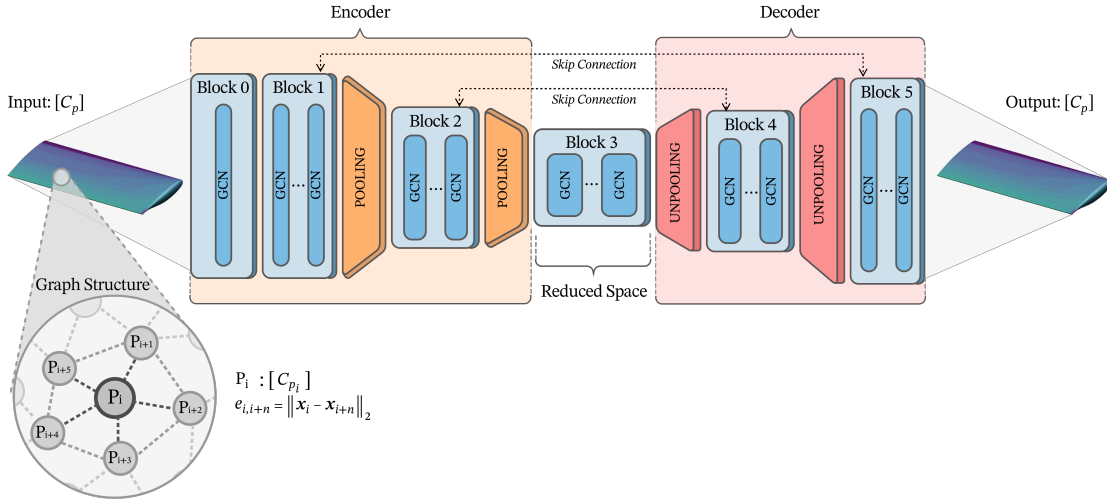


Figure 3: Schematic of the pre-trained AE architecture for compressing and reconstructing the C_P data within the GST GraphNet framework.

3. Test Case

The selected case study for evaluating our framework is the Benchmark Super Critical Wing (BSCW), a transonic rigid semi-span wing featuring a rectangular planform and a supercritical airfoil profile, as detailed in the AIAA Aeroelastic Prediction Workshop [45]. The freestream conditions for this case are defined by a Mach number of 0.74, a Reynolds number of 4.49×10^6 , and an initial angle of attack of 0 degree. The wing features a reference chord length of 0.4064 *m* and a surface area of 0.3303 *m*², with pitching motion occurring around 30% of the chord. It is mounted on a flexible support system that allows two degrees of freedom: pitch θ and plunge ξ . It is designed for flutter analysis, presenting challenges due to shock wave motion, shock-induced boundary-layer separation, and the interaction between the shock wave and the detached boundary layer. These nonlinear phenomena pose significant challenges for the framework predictions.

An unstructured mesh with 8.4×10^6 elements and 86,840 surface elements was created. A $y^+ = 1$ value was used, based on a preliminary mesh convergence study that confirmed adequate resolution of the boundary layer and shock wave. The computational domain extends 100 chord lengths from the solid wall to the farfield. Figure 4 provides an impression of the mesh configuration.

The dataset used to train the model was generated with CFD unsteady responses using the Unsteady Reynolds-averaged Navier–Stokes (URANS) formulation with SU2 v7.5.1 [46]. The simulations employed the one-equation Spalart-Allmaras turbulence model for RANS closure. To accelerate convergence, a 1*v* multigrid scheme was used. The JST central scheme with artificial dissipation handled convective flow discretization, and the gradients of flow variables were calculated using the Green-Gauss method. The biconjugate gradient stabilization linear solver, along with the ILU preconditioner, was utilized. All URANS simulations started from a steady-state solution, with a timestep of 2×10^{-4} seconds and a total simulation time of 2 seconds. These values were chosen to ensure a high temporal resolution, capturing rapid aerodynamic variations while keeping the computational cost manageable over the full simulation period. However, due to computational constraints, the timestep was reduced to 2×10^{-3} seconds through downsampling for model training, ensuring a balance between computational feasibility and quality of aerodynamic data.

We ran a total of 12 time-varying simulations, divided into training, test, and validation sets as described in Table 3. The training set comprises damped Schroeder-phased harmonic (DS) simulations (see Appendix A for details on the DS signal formulation) with varied combinations of the parameters: reduced frequency for pitch (κ_θ), maximum pitch amplitude (a_θ), reduced frequency for plunge (κ_ξ), and maximum plunge amplitude (a_ξ), ensuring that the model learns from diverse con-

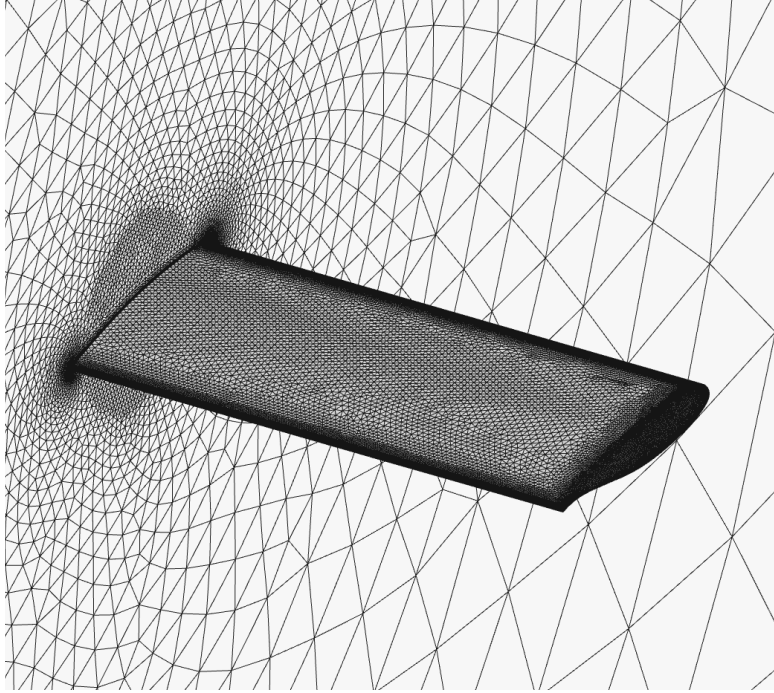


Figure 4: Impression of the BSCW CFD grid.

ditions where these variables exhibit both positive and negative values (Figure 5). This variation helps the model understand the complex interactions between the parameters. The test set extends this diversity by including additional combinations and signal types, specifically undamped Schroeder-phased harmonic (US) and cases focusing solely on θ or ξ variations. This approach allows us to accurately assess the model accuracy and sensitivity in predicting the effects of individual parameters, ensuring that it performs well across different conditions. The use of Schroeder signals is motivated by their ability to effectively cover a broad frequency spectrum while minimizing peak amplitudes, which enhances the model robustness and ability to generalize. The validation set is designed to evaluate the model generalizability to new and unseen data. It includes a scenario similar to those in the training set but with distinct parameter values, as well as a unique single harmonic (SH) signal type, which the model did not encounter during training. This ensures that the model can handle both familiar and novel situations effectively.

Signals	κ_θ [-]	a_θ [deg]	κ_ξ [-]	a_ξ [m]	Type
Training 1	0.114	0.80	0.152	-0.098	DS, $\theta > 0$, $\xi < 0$
Training 2	0.114	-0.80	0.152	0.098	DS, $\theta < 0$, $\xi > 0$
Training 3	0.148	1.00	0.181	-0.123	DS, $\theta > 0$, $\xi < 0$
Training 4	0.148	-1.00	0.181	0.123	DS, $\theta < 0$, $\xi > 0$
Test 1	0.091	0.70	0.123	0.074	DS, $\theta > 0$, $\xi > 0$
Test 2	0.104	0.90	0.089	0.061	DS, $\theta > 0$, $\xi < 0$
Test 3	0.104	-0.90	0.089	-0.061	DS, $\theta < 0$, $\xi < 0$
Test 4	0.092	0.75	0.081	-0.059	US, $\theta > 0$, $\xi < 0$
Test 5	0.147	-1.00	0.000	0.000	DS, $\theta < 0$
Test 6	0.000	0.00	0.072	0.049	DS, $\xi > 0$
Validation 1	0.147	-1.00	0.072	0.049	DS, $\theta < 0$, $\xi > 0$
Validation 2	0.106	3.00	0.089	-0.246	SH, $\theta > 0$, $\xi < 0$

Table 3: Parameters and types of training, test and validation signals. DS: damped Schroeder-phased harmonic, US: undamped Schroeder-phased harmonic, SH: single harmonic.

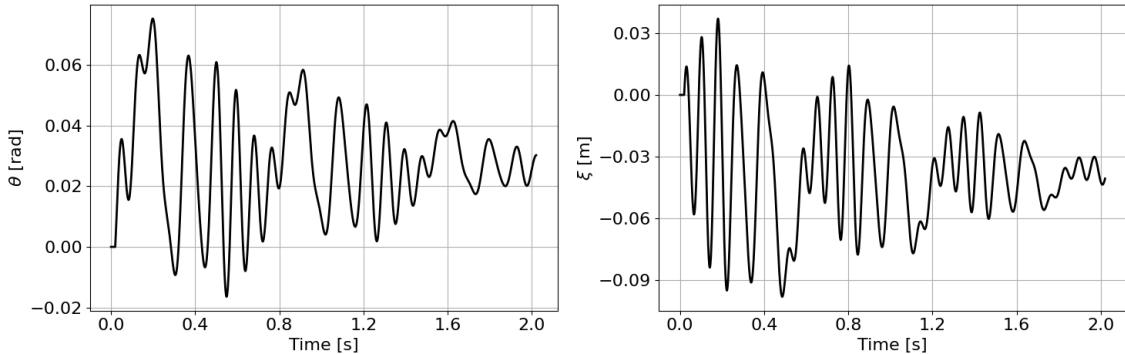


Figure 5: Training signal 1: DS with $\kappa_\theta = 0.114$, $a_\theta = 0.80$ [deg], $\kappa_\xi = 0.152$, and $a_\xi = -0.098$ [m].

4. Results

In this section, we present the results of the reconstructed validation signals for two different types of architectures: feedforward model and ARMAX model. By comparing the performance of these two architectures, we aim to illustrate the influence of incorporating predicted C_P into the model input on the overall prediction accuracy and robustness. The impact of the temporal layer on the accuracy of each architecture is also studied.

4.1. Feedforward Model

The feedforward model utilizes spatial and temporal data from previous timesteps without relying on its own past predictions, thus preventing the accumulation of errors over time. The model performance across different temporal layers is evaluated using both DS and SH validation signals.

For the DS signal (Figures 6 and 7), the predictions of the aerodynamic coefficients C_L and C_M align well with the CFD reference data in all temporal layers, as shown in Figure 6. The STGCN layer demonstrates the lowest average error for C_L , while LSTM performs slightly better for C_M . A region of maximum error, indicated by the red circle, is consistent across all models and represents the point where the predictions for C_L and C_M show the greatest deviation from the reference data. This error appears to be related to the models difficulty in capturing sharp transitions or non-linearities in the aerodynamic flow, particularly near shock waves. Figure 7 shows the C_P distribution at this maximum error point and highlights the models overall ability to predict the pressure distribution across the wing. While most temporal layers perform reasonably well, some discrepancies near the leading edge and areas affected by shock waves and flow separation are noticeable. These areas, characterized by strong flow gradients and non-linear aerodynamic behavior, are challenging for all models, although STGCN and LSTM exhibit slightly better accuracy compared to GRU and Attention mechanisms.

For the SH signal (Figures 8 and 9), which involves higher-frequency oscillations, the models encounter increased errors, particularly in predicting peak values for C_L and C_M . LSTM and STGCN continue to provide the most accurate results, although both exhibit some phase and amplitude errors due to the rapid oscillations. The red-circled point, indicating the region of maximum error for C_L and C_M , again highlights the challenges of accurately capturing high-frequency aerodynamic loads. Figure 9 provides a detailed view of the C_P distribution at this maximum error point, where the models struggle more to match the rapid fluctuations in C_P . In particular, regions near the shock wave, which undergo significant temporal variation, show greater discrepancies. While the general C_P distribution is captured, the accuracy decreases in areas where shock-induced flow separation occurs, with LSTM and STGCN again showing marginally better performance in these challenging regions.

To quantitatively evaluate the models, we calculated three error metrics—Mean Absolute Percentage Error (MAPE), coefficient of determination (R2), and Root Mean Square Error (RMSE)—for C_P predictions across both validation signals, as shown in Table 4. The MAPE was derived by averaging the absolute errors across each timestep, weighted by the corresponding cell area, and normalized accordingly. It reflects the average percentage error across predictions, showing that the LSTM model consis-

tently achieves the lowest values, while the STGCN model follows closely. GRU and Attention mechanisms, on the other hand, display significantly higher MAPE, particularly for the high-frequency oscillations of the SH signal, indicating their difficulty in capturing rapid temporal variations and non-linearities. In terms of R2, which measures how well the model explains variance in the data, LSTM again performs the best, capturing the highest degree of variability, followed closely by STGCN, which also demonstrates strong performance in the DS signal but slightly lower accuracy for the SH signal. GRU and Attention layers show lower R2, further confirming their difficulty to fully capture the complexities in regions involving shock waves and high dynamic variability. Regarding RMSE, which emphasizes larger errors due to its quadratic nature, the LSTM model continues to perform better with the lowest values, indicating a good robustness against significant deviations. STGCN performs similarly but struggles slightly more with large deviations in dynamic conditions like the SH signal. Again, GRU and Attention mechanisms exhibit the highest RMSE.

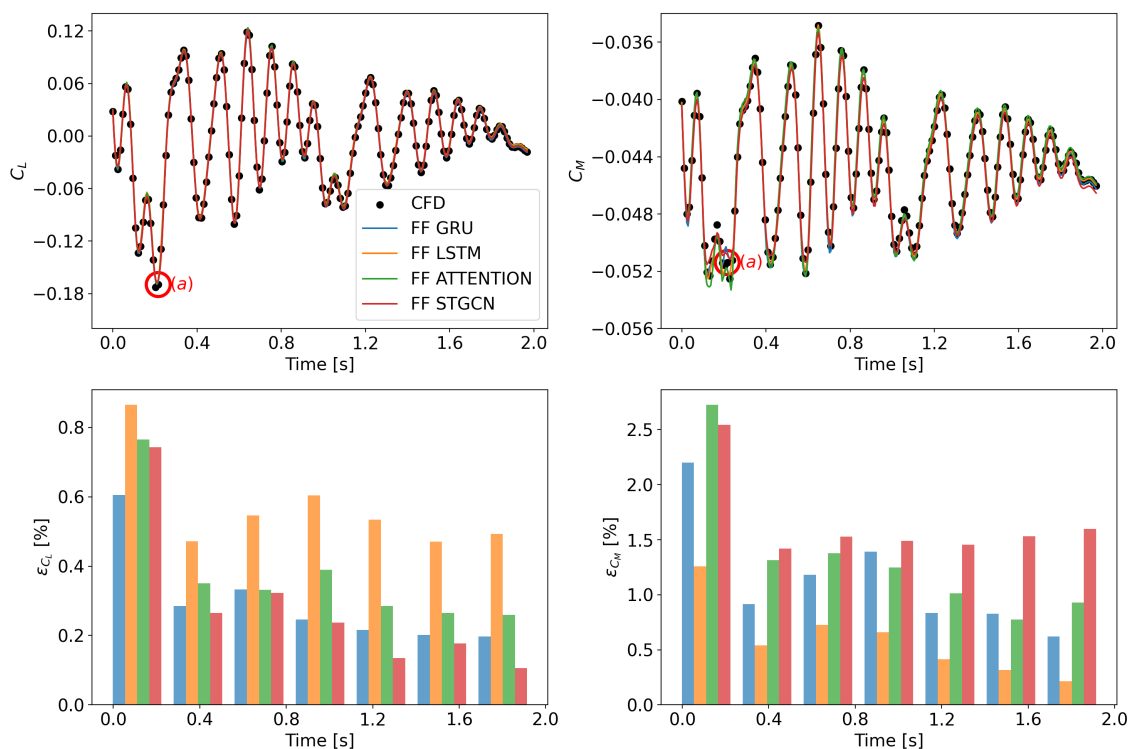


Figure 6: Validation signal 1 - DS type: Effect of temporal layer selection on C_L and C_M predictions in the feedforward model. The red circle marks the point of maximum error, used for plotting the C_P distribution. FF: FeedForward.

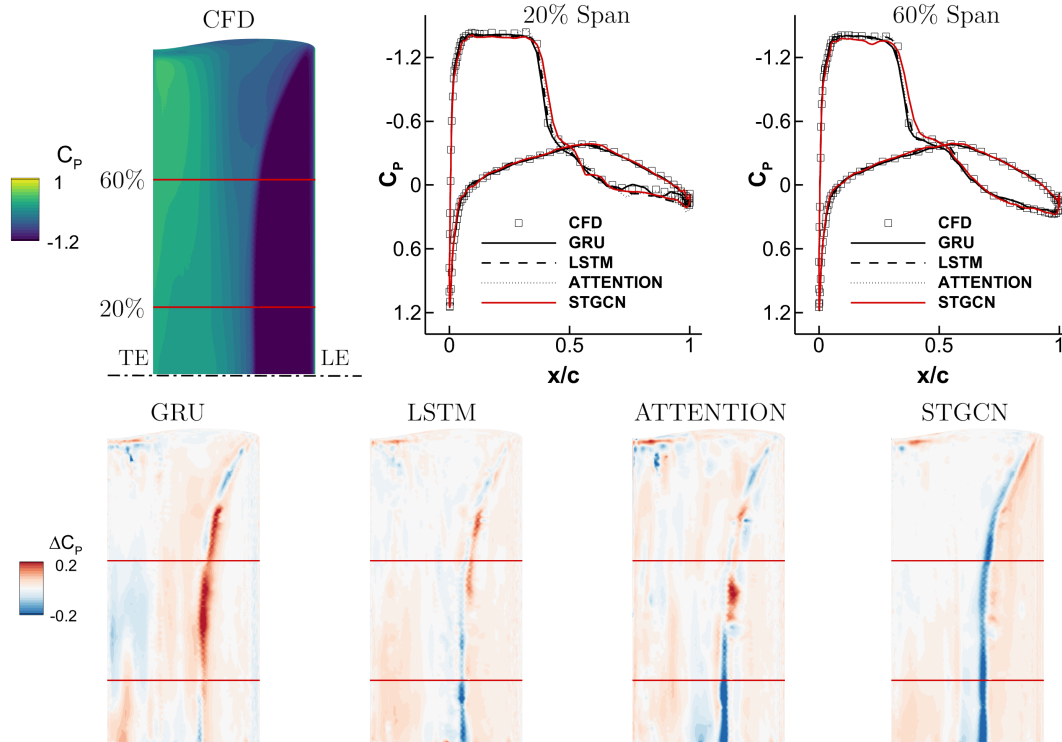


Figure 7: Validation signal 1 - DS type: Effect of temporal layer selection on C_P prediction at the maximum error point in the feedforward model. The lower surface of the wing is shown. LE: Leading Edge. TE: Trailing Edge. Dash-dot line indicates the symmetry plane.

These results suggest that all models are well-suited for capturing both spatial and temporal dependencies with good overall performance, but GRU and Attention layers struggle more to capture the rapid temporal variations and non-linearities in the C_P distribution.

In conclusion, while all temporal layers provide reasonable predictions for unsteady aerodynamic phenomena, the LSTM model delivers the most robust performance across both validation signals. STGCN also performs well, particularly for C_L predictions, while GRU and Attention mechanisms exhibit larger errors, especially in more complex dynamics. The evaluation of C_P distribution highlights the importance of accurately capturing non-linear flow features, with regions near shock waves and flow separations proving to be the most challenging for all models.

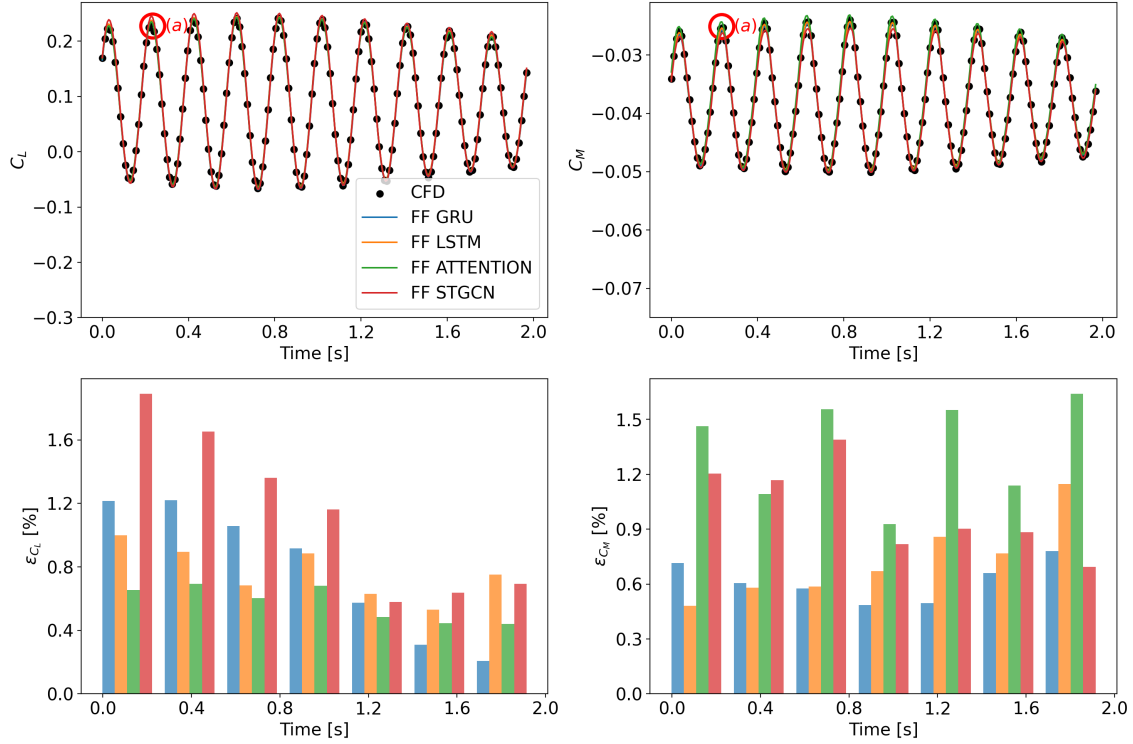


Figure 8: Validation signal 2 - SH type: Effect of temporal layer selection on C_L and C_M predictions in the feedforward model. The red circle marks the point of maximum error, used for plotting the C_P distribution. FF: FeedForward

Temporal Layer	MAPE		R2		RMSE	
	DS	SH	DS	SH	DS	SH
GRU	1.2382	1.7851	0.9851	0.9830	0.0217	0.0229
LSTM	0.7471	0.9695	0.9937	0.9909	0.0194	0.0215
Attention	1.0470	1.5452	0.9887	0.9815	0.0238	0.0291
STGCN	0.8524	0.9975	0.9918	0.9897	0.0163	0.0181

Table 4: Comparison of MAPE, R2, and RMSE for C_P predictions in the feedforward model with different temporal layers for DS and SH validation signals.

4.2. ARMAX Model

The ARMAX model, which integrates past predictions into its input, was evaluated using various temporal layers to assess its performance in predicting C_L , C_M , and C_P across DS and SH validation signals. As shown in Figure 10, one of the biggest limitations of the ARMAX model consists of accumulation of errors over

time, particularly when using the GRU and Attention mechanisms. Again, LSTM and STGCN demonstrate better predictive performance, although both exhibit some deviations in complex flow regions. The red-circled points were selected to visualize the evolution of the error over time. These points were spaced at regular intervals along the signal to provide insight into how prediction accuracy changes throughout the sequence. This allows us to observe how the model handles different stages of prediction and highlights its difficulty in accurately capturing sharp transitions and non-linearities in the aerodynamic flow, particularly around shocks. This issue is further emphasized in Figure 11, where the C_P at these selected points shows that the ARMAX model has more difficulty maintaining accuracy near the leading edge and in shock-affected regions. Despite these challenges, LSTM and STGCN continue to provide the most reliable predictions despite the inherent error accumulation.

For the SH signal (Figures 12 and 13), which involves higher frequency oscillations,

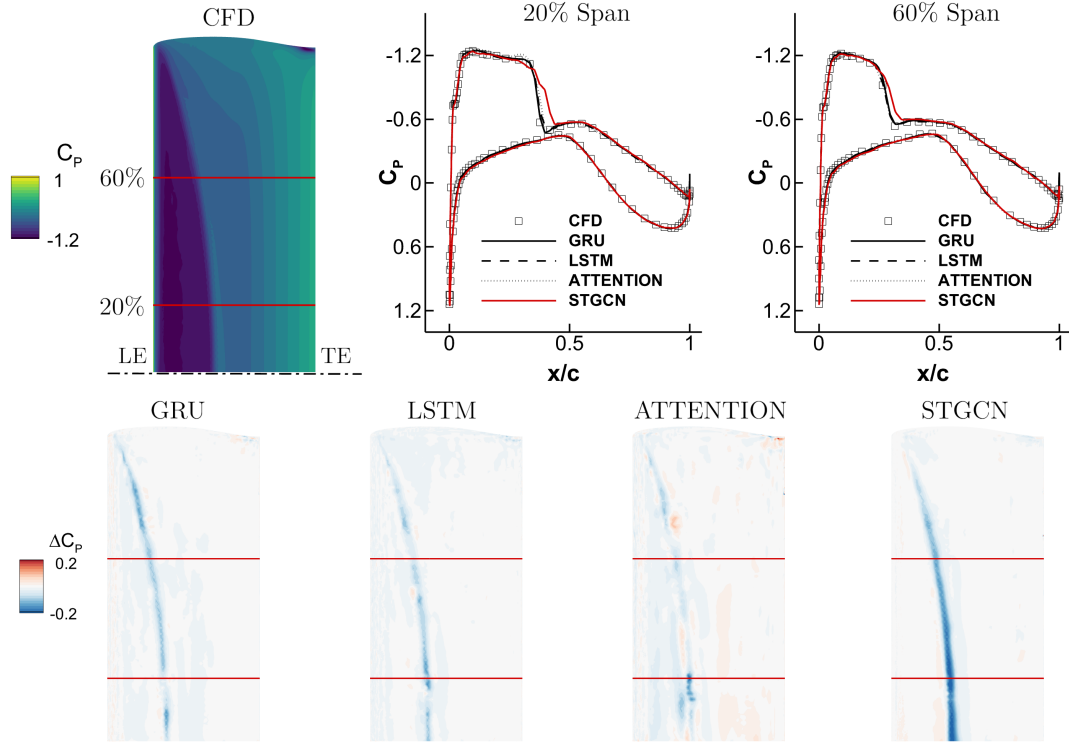


Figure 9: Validation signal 2 - SH type: Effect of temporal layer selection on C_P prediction at the maximum error point in the feedforward model. The upper surface of the wing is shown. LE: Leading Edge. TE: Trailing Edge. Dash-dot line indicates the symmetry plane.

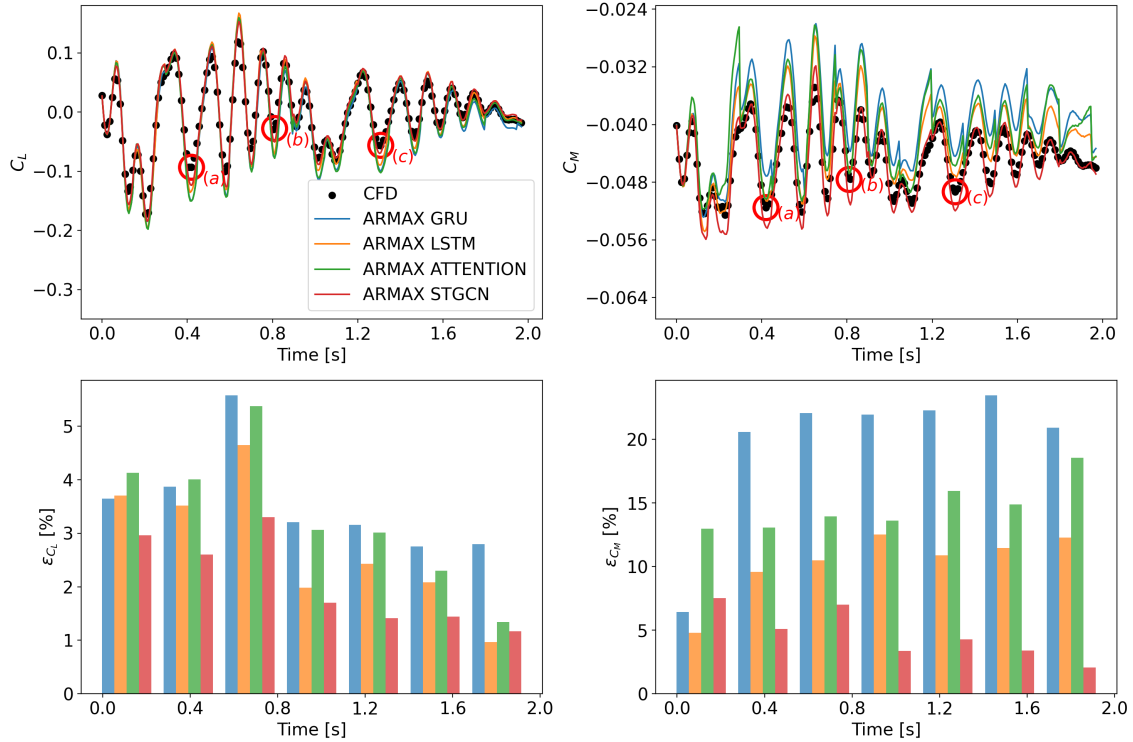
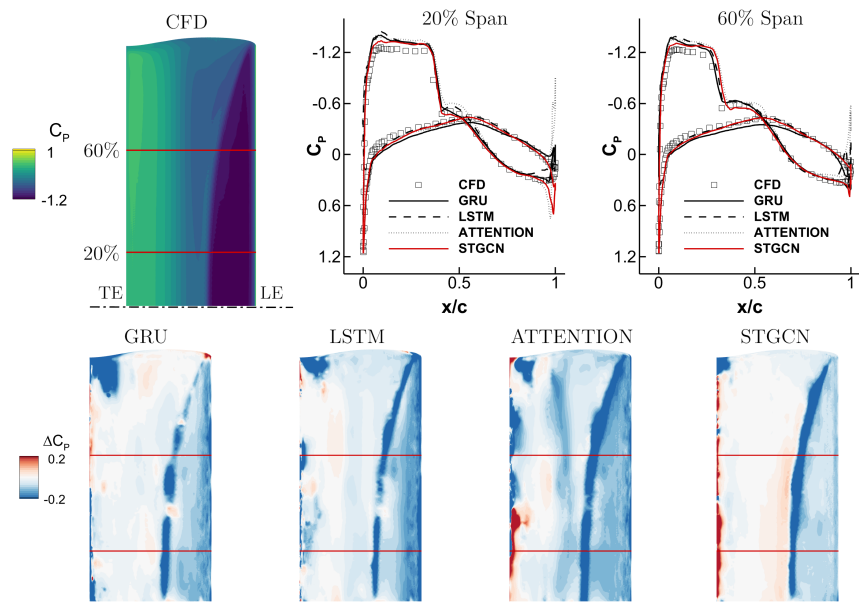


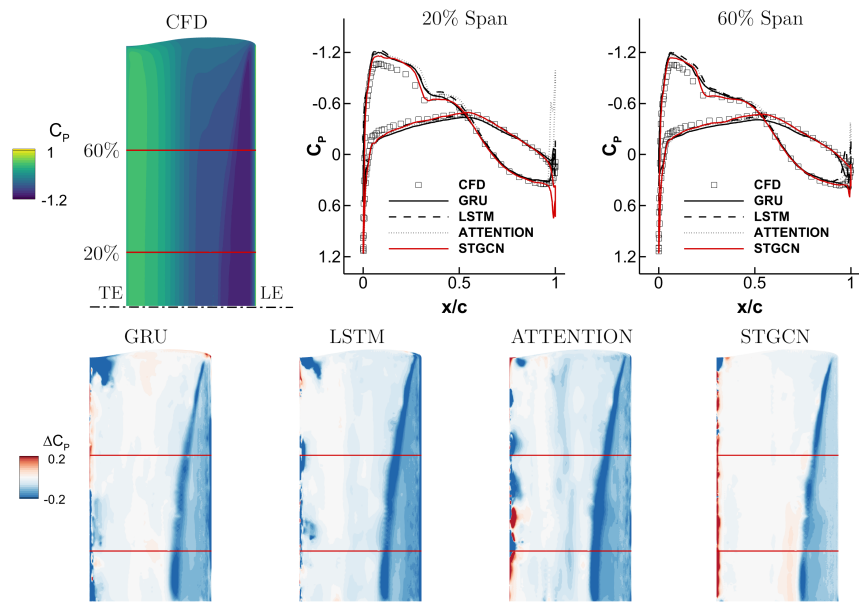
Figure 10: Validation signal 1 - DS type: Impact of temporal layer selection on C_L and C_M predictions in the ARMAX model. Red circles denote the points used for plotting the C_P distribution.

tions, the ARMAX model exhibits increased errors, particularly for the GRU and Attention layers. The rapid oscillations introduce phase and amplitude discrepancies, with LSTM and STGCN handling these variations better, though both models still show increased errors compared to the DS signal. The C_P distribution in Figure 13 reveals that the ARMAX model is more susceptible to error propagation in highly dynamic regions near shock waves, where rapid changes in flow introduce greater inaccuracies. Although LSTM and STGCN mitigate these issues to some extent, they still experience some degradation in predictive accuracy due to the model autoregressive nature.

The superior performance of LSTM and STGCN can be attributed to their inherent design, which allows them to handle temporal dependencies more effectively. The LSTM architecture, with its complex gating mechanisms, enables the model to retain and manage both long- and short-term dependencies, preventing information loss over multiple timesteps and helping to mitigate the error accumulation issue inherent in the ARMAX model. The STGCN layer combines both spatial and tem-



Time Instance (a)



Time Instance (b)

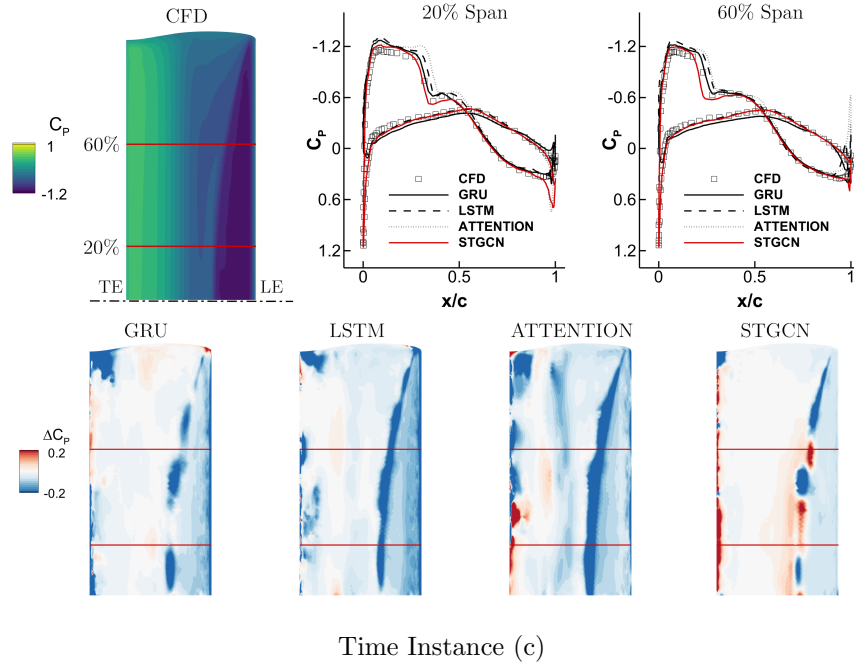


Figure 11: Validation signal 1 - DS type: Impact of temporal layer selection on C_P prediction at the maximum error point in the ARMAX model. The lower surface of the wing is shown. LE: Leading Edge. TE: Trailing Edge. Dash-dot line indicates the symmetry plane.

poral convolutions, making it well-suited to handle non-uniform grid structures and effectively capture spatial correlations (such as pressure gradients across the wing) as well as temporal dependencies during rapid changes in aerodynamic conditions, as seen in the SH signal.

In contrast, the GRU simpler structure limits its capacity to capture long-term dependencies effectively. The Attention mechanism, while effective for capturing important temporal relationships in longer sequences, is not as well suited to the short input sequences used in this model, where the benefits of dynamically weighting timesteps are reduced, limiting the Attention layer effectiveness.

Table 5 quantifies the performance of the different temporal layers in terms of MAPE, R2, and RMSE for C_P predictions in the ARMAX model. The STGCN model consistently achieves the lowest MAPE and RMSE values across both the DS and SH signals, with LSTM performing nearly as well. This suggests that both models are adept at handling temporal dependencies even in autoregressive contexts, although the STGCN slightly outperforms LSTM, particularly in the dynamic SH signal. GRU

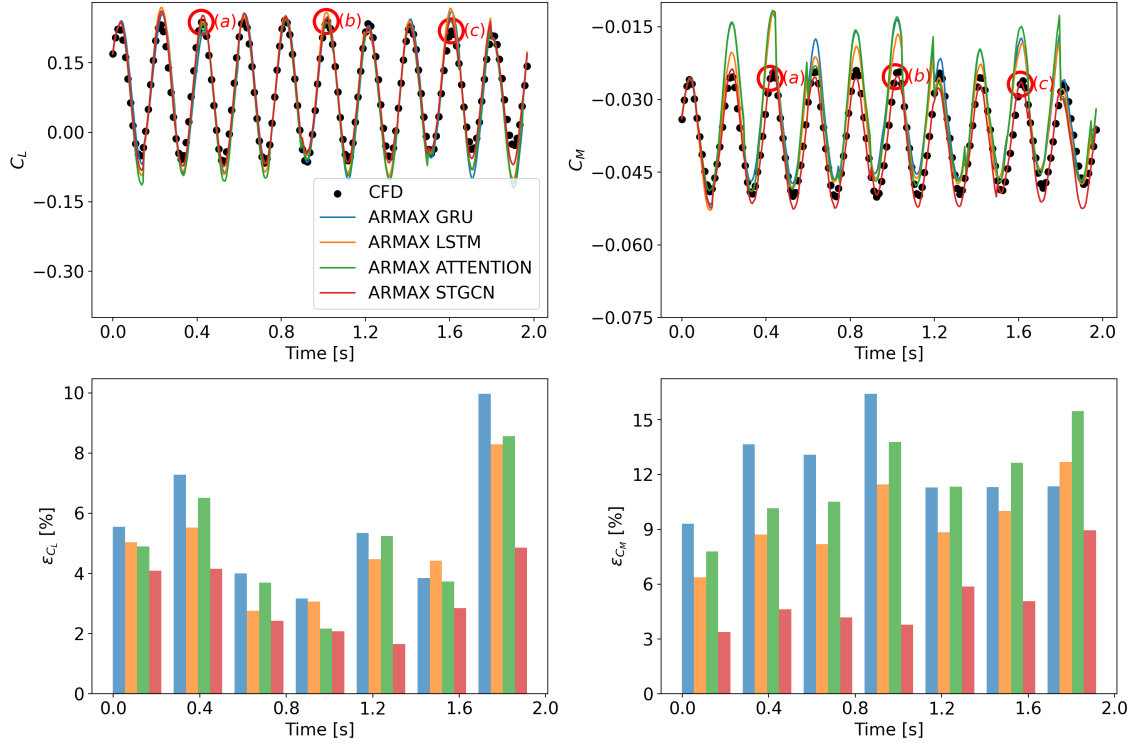
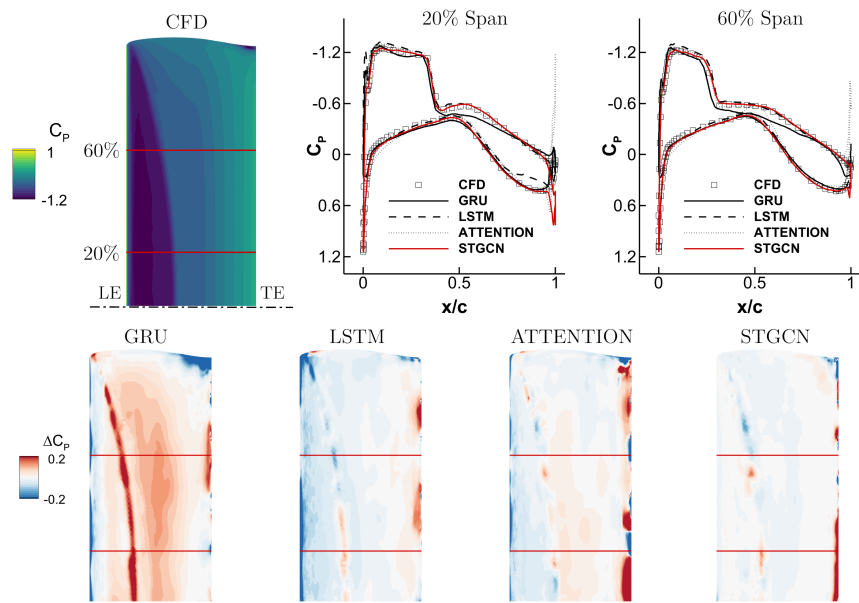


Figure 12: Validation signal 2 - SH type: Impact of temporal layer selection on C_L and C_M predictions in the ARMAX model. Red circles denote the points used for plotting the C_P distribution.

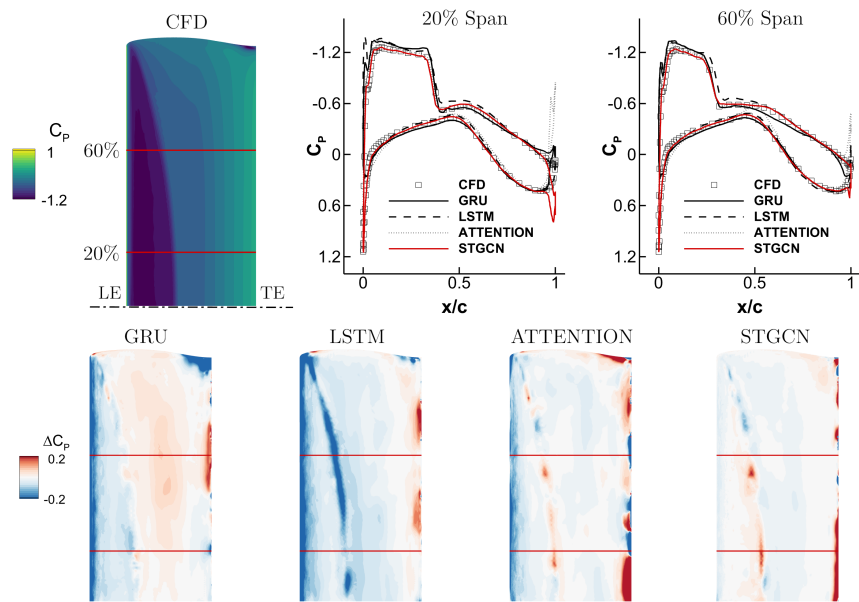
and Attention layers, on the other hand, show higher MAPE and RMSE, along with lower R2, indicating that they struggle to mitigate the error accumulation inherent in the ARMAX model, particularly in high-frequency oscillations. The lower R2 values for GRU and Attention mechanisms highlight their reduced ability to capture the full variability in the data with rapid aerodynamic changes. Overall, the results suggest that while the ARMAX model can capture general trends, its susceptibility to error propagation makes it crucial to use robust temporal layers, such as LSTM and STGCN, to minimize predictive inaccuracies in highly dynamic and non-linear aerodynamic conditions.

4.3. Feedforward vs ARMAX

The comparison between ARMAX and feedforward models, both using the STGCN temporal layer, reveals notable differences in performance, especially regarding error accumulation and prediction stability. The STGCN temporal layer was selected for this comparison because it consistently yielded the most accurate results across both



Time Instance (a)



Time Instance (b)

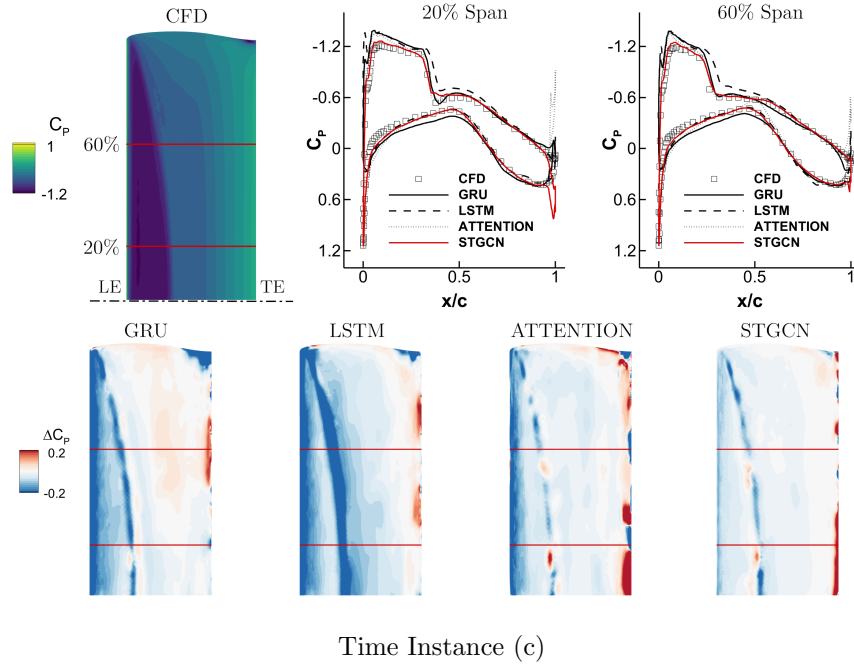


Figure 13: Validation signal 2 - SH type: Impact of temporal layer selection on C_P prediction at the maximum error point in the ARMAX model. The upper surface of the wing is shown. LE: Leading Edge. TE: Trailing Edge. Dash-dot line indicates the symmetry plane.

Temporal Layer	MAPE		R2		RMSE	
	DS	SH	DS	SH	DS	SH
GRU	8.5577	6.7837	0.7560	0.7993	0.1389	0.1439
LSTM	7.7511	6.4299	0.8426	0.8506	0.1002	0.0864
Attention	7.7985	5.8077	0.8167	0.7796	0.1233	0.1048
STGCN	6.9381	5.7971	0.8571	0.8648	0.0938	0.0844

Table 5: Comparison of MAPE, R2, and RMSE for C_P predictions in the ARMAX model with different temporal layers for DS and SH validation signals.

validation signals, as demonstrated in previous sections. In this case, ARMAX model uses ground-truth C_P values for the first half of the signal, after which it switches to using its own predictions for subsequent timesteps. As shown in Figure 14, the feed-forward model provides more accurate predictions for C_L and C_M on the DS signal, avoiding the accumulation of errors observed in the ARMAX model. The red circled points were chosen to be in the middle of the first and second halves of the signal,

providing information on the behavior of the model during the transition from using ground truth to self-predicted values. This choice allows for a clearer comparison of model performance during both phases, highlighting the ARMAX model difficulty in limiting error accumulation, while the feedforward model maintains closer alignment with the reference data. This trend is further confirmed in Figure 15, where the evolution of the MAPE in C_P reveals that the feedforward model consistently maintains lower error levels over time compared to the ARMAX model, which, as expected, shows a clear pattern of accumulation of errors.

Interestingly, the ARMAX model performs relatively well during the first half of the signals, when ground-truth C_P values are used as input. In this phase, the ARMAX model can even outperform the feedforward model, as seen in the initial part of Figures 14 and 15. However, once the model begins using its own predicted C_P values for subsequent timesteps, error accumulation begins, resulting in larger deviations from the reference data. This behavior is clearly seen in Figure 16, where the ARMAX model shows growing discrepancies in C_P predictions as the autoregressive process progresses. In contrast, the feedforward model avoids this problem by not relying on its past predictions, allowing it to maintain better accuracy in regions near the leading and trailing edges, where flow complexity is higher.

These trends are even more evident with the SH signal, which features rapid oscillations. Figure 17 shows that the feedforward model handles these high-frequency aerodynamic variations more effectively, with significantly fewer phase and amplitude errors than the ARMAX model. The ARMAX model, due to its time-marching scheme, exhibits a greater sensitivity to reduced frequency. At higher frequencies, errors accumulate faster as small inaccuracies from previous steps compound. Once the ARMAX model switches from using ground-truth inputs to its own predictions, it fails to keep pace with the rapid changes in aerodynamic forces, resulting in larger phase lags and more significant deviations from the reference data. In contrast, as the feedforward model relies only on the wing spatial coordinates and prescribed motions at previous timesteps (without feeding back its own predictions), it results in a more stable error profile and in a more reliable and accurate predictions of unsteady phenomena.

As shown in Figure 18, the feedforward model consistently outperforms the ARMAX model in terms of MAPE on C_P for the SH signal. The ARMAX model error accumulation is particularly pronounced in more dynamic conditions, such as rapid oscillations, which results in significantly higher MAPE. Figure 19 further supports this observation, showing that the feedforward model is better at predicting the C_P distribution, where the ARMAX model struggles due to the accumulation of prediction errors. However, it is important to note that when the ARMAX model is fed with

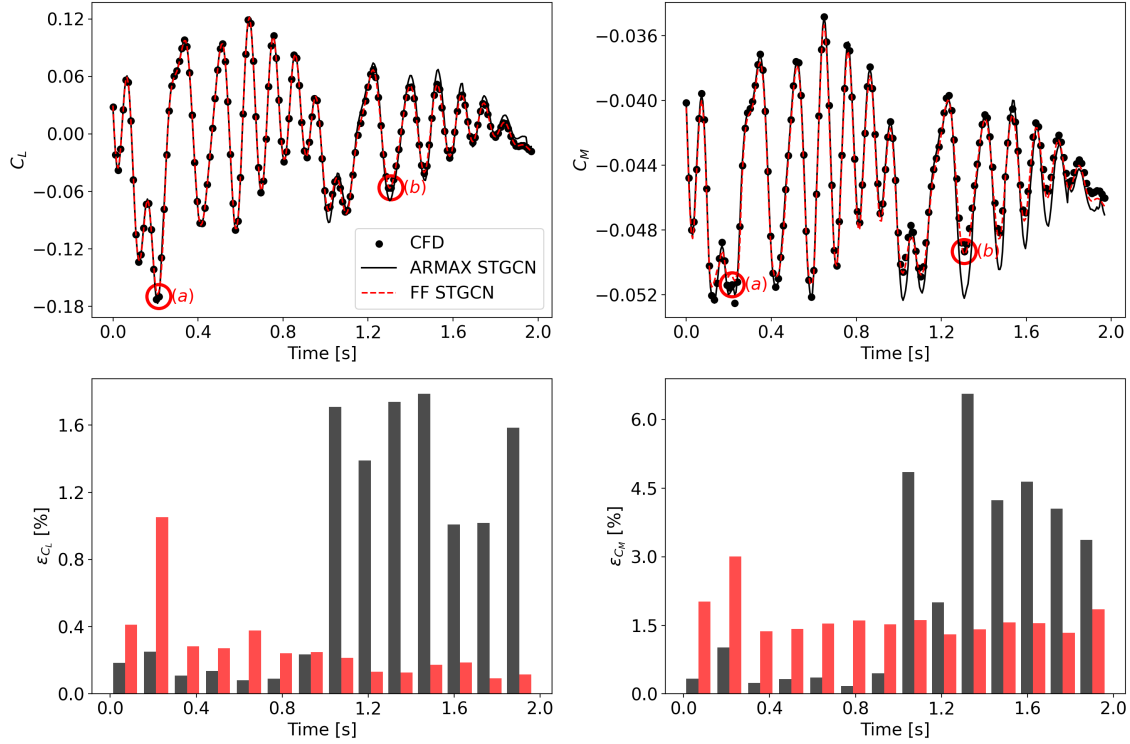


Figure 14: Validation signal 1 - DS type: ARMAX vs Feedforward model using STGCN temporal layer on C_L and C_M predictions. Red circles denote the points used for plotting the C_P distribution.

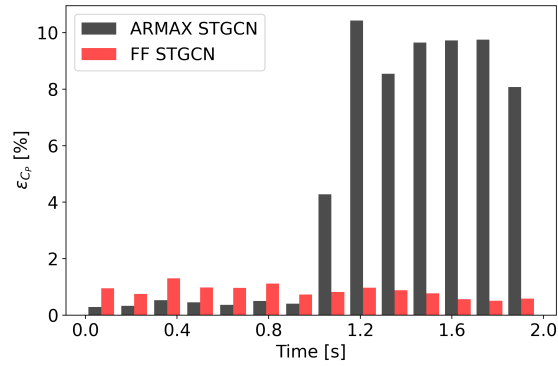
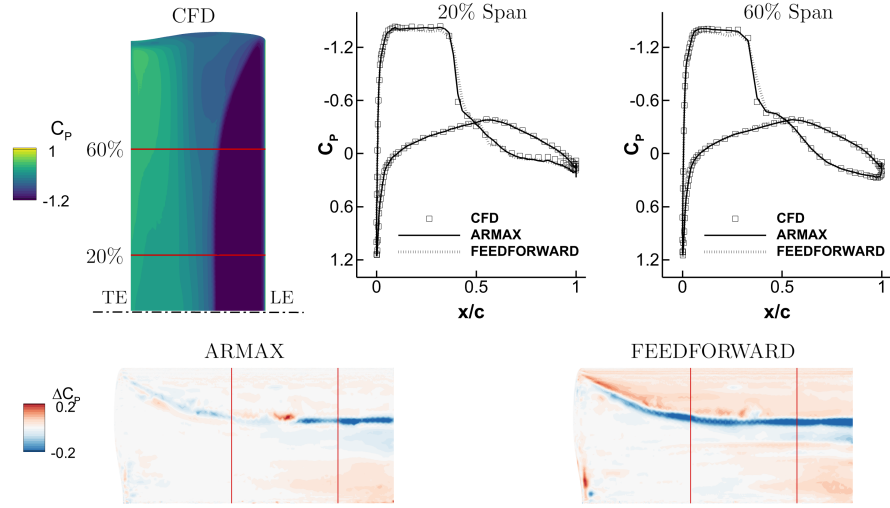
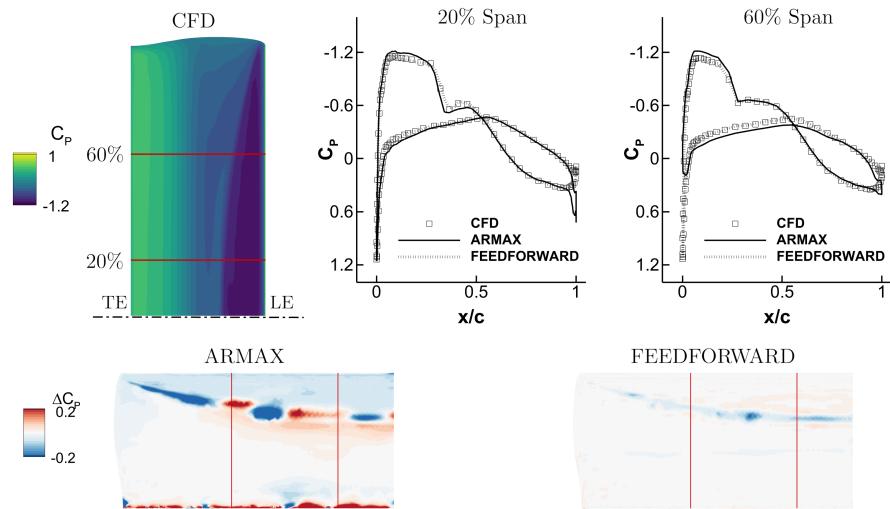


Figure 15: Validation signal 1 - DS type: Evolution of MAPE of C_P with ARMAX and Feedforward model.

ground-truth C_P values, it can produce very accurate predictions, outperforming the feedforward model. This highlights the ARMAX potential in study cases where error



Time Instance (a)



Time Instance (b)

Figure 16: Validation signal 1 - DS type: ARMAX vs Feedforward model using STGCN temporal layer on C_P prediction. The lower surface of the wing is shown. LE: Leading Edge. TE: Trailing Edge. Dash-dot line indicates the symmetry plane.

on pressure values does not accumulate too fast, as in systems with lower reduced

frequency. Also, insufficient convergence of the CFD solution may affect error accumulation in regions with complex flow patterns, suggesting that improving solution stability may help mitigate this problem.

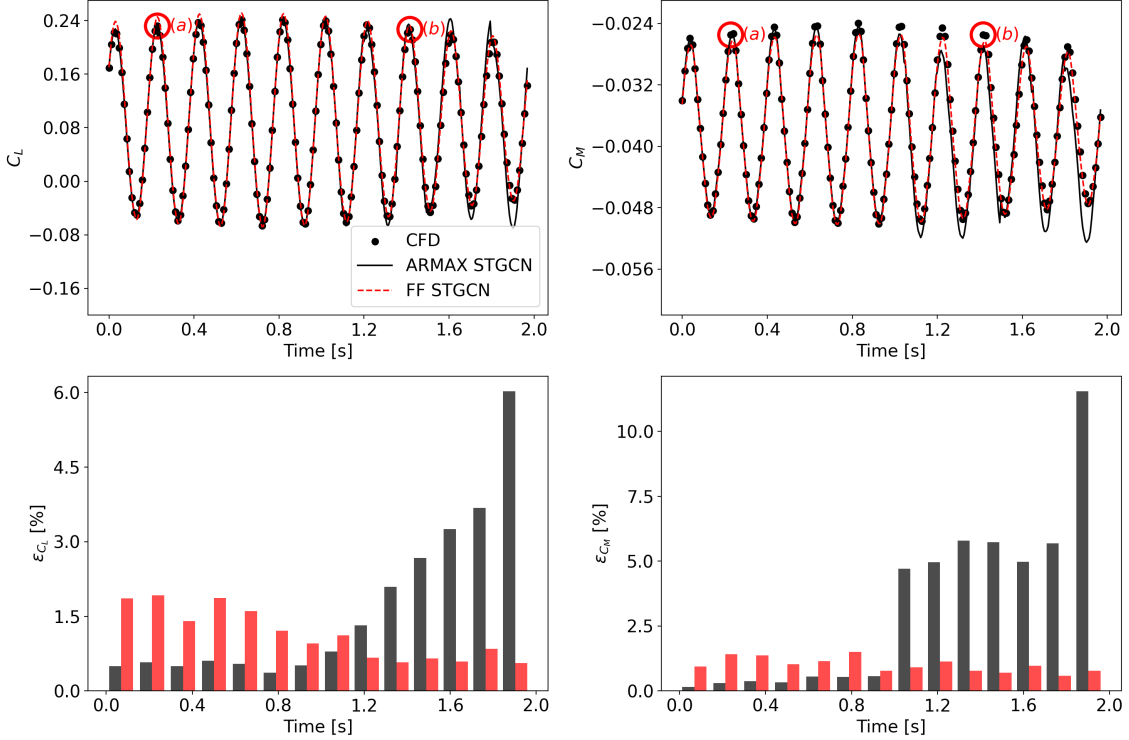


Figure 17: Validation signal 2 - SH type: ARMAX vs Feedforward model using STGCN temporal layer on C_L and C_M predictions. Red circles denote the points used for plotting the C_P distribution.

4.4. Computing Cost Analysis

A comprehensive analysis of computational costs was performed to compare the efficiency of the proposed model with that of a higher-order approach, as shown in Table 6. A single CFD run on a high-performance computing system, using an Intel Skylake-based architecture with 3 nodes and 40 CPU cores per node, typically requires around 6,000 CPU hours. Generating the entire dataset demands approximately 75,000 CPU hours. In contrast, the proposed framework allows predictions for a single sample on a local machine with a NVIDIA RTX A4000 GPU to be completed in roughly two minutes, leading to computational savings of over 99%. Nonetheless, it is important to acknowledge the substantial computational effort involved in generating the high-fidelity simulations used to create the dataset. This

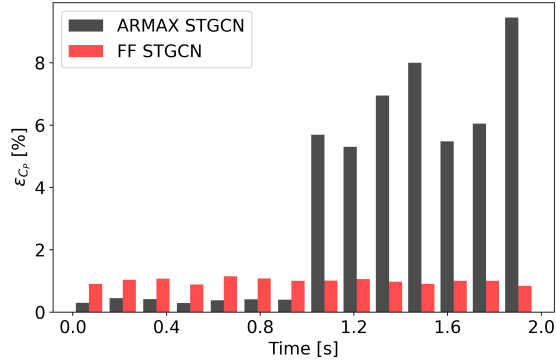
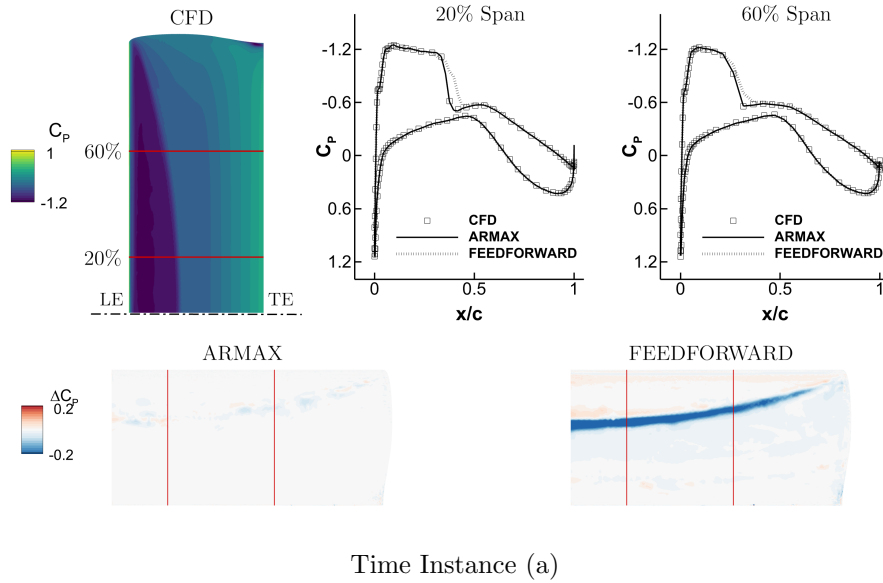


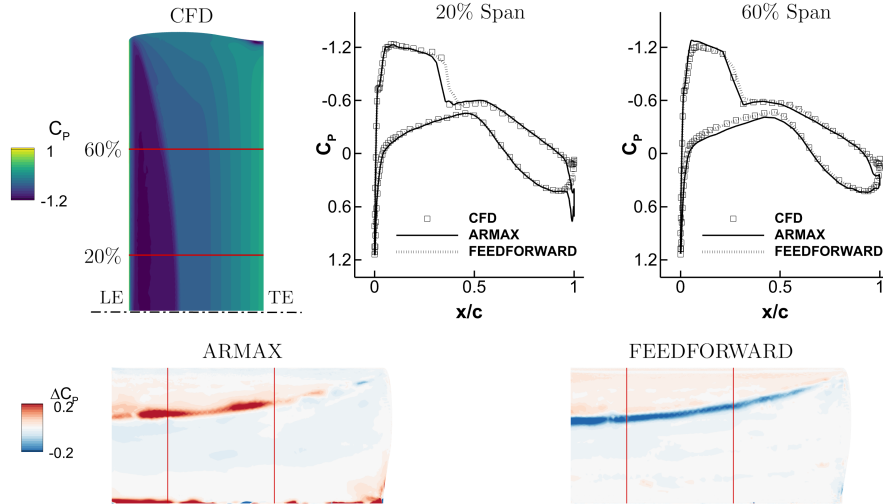
Figure 18: Validation signal 2 - SH type: Evolution of MAPE of C_p with ARMAX and Feedforward model.



underscores the need for strategies that reduce the amount of training data required to develop an accurate model.

5. Conclusions

This study introduced a framework for predicting unsteady transonic wing pressure distributions, integrating an AE architecture with GCN and graph-based temporal layers to capture time dependencies. The proposed model effectively compresses high-dimensional C_p distribution data into a lower-dimensional latent space using



Time Instance (b)

Figure 19: Validation signal 2 - SH type: ARMAX vs Feedforward model using STGCN temporal layer on C_P prediction. The upper surface of the wing is shown. LE: Leading Edge. TE: Trailing Edge. Dash-dot line indicates the symmetry plane.

CFD (CPU hours)		GST GraphNet (GPU hours)				
Simulation (12 runs)	(1 run)	Pre-Trained AE (Optimization + Training)	Training (ARMAX)	(FF)	Prediction (ARMAX)	(FF)
75,000	6,000	42.6	35.2	33.1	0.03	0.03

Table 6: Computing cost comparison between GST GraphNet model and CFD. FF: FeedForward.

the AE, preserving essential features for accurate representation. The GCN layers are well-suited for handling the unstructured grids characteristic of aerodynamic data, while the temporal layers capture and leverage temporal dependencies for robust forecasting of wing C_P distributions.

Our results demonstrated that this integrated approach can achieve an accuracy comparable to traditional CFD methods, while significantly reducing computational costs. We evaluated two architectures, the feedforward model and the ARMAX model, using different temporal layers, with the STGCN layer consistently delivering the most accurate results across the validation signals. The feedforward model demonstrated clear advantages in terms of predictive accuracy and stability, partic-

ularly in avoiding the error propagation inherent in the ARMAX model. By not relying on its own predictions for subsequent inputs, the feedforward model is better suited for both steady and highly dynamic aerodynamic conditions, showing greater accuracy in predicting complex flow features, such as shock waves and flow separation. The ARMAX model, while capable of capturing general trends, is more prone to error accumulation, particularly in scenarios with high-frequency oscillations or rapid changes in aerodynamic forces. Nonetheless, when using ground-truth inputs, the ARMAX model can yield highly accurate results, underscoring its potential in scenarios with reliable data inputs.

Future work will focus on extending the framework to different flight regimes to validate its adaptability to a wider range of aerodynamic conditions. Additionally, scalability to larger grids and different graph structures will be explored. GCNs inherently support various graph configurations, but expanding the model to handle new spatial structures or larger meshes may require techniques like subgraph splitting or padding to ensure stable performance. As grid size increases, deeper networks and additional pooling layers will be necessary to capture long-range dependencies efficiently, while maintaining computational feasibility.

Acknowledgement

This work was supported by Digitalization Initiative of the Zurich Higher Education Institutions (DIZH) grant from Zurich University of Applied Sciences (ZHAW). The authors also acknowledge the University of Southampton for granting access to the IRIDIS High Performance Computing Facility and its associated support services.

Appendix A. Schroeder-Phased Harmonic Signal Formulation

The Schroeder-phased harmonic signal is utilized in this study to improve the robustness and generalizability of the model by covering a wide frequency spectrum. These signals are constructed by summing sinusoidal components, where the phases are optimized to minimize the overall peak amplitude. This results in an evenly distributed energy spectrum, which is advantageous for training the model to handle various frequency interactions and reduces the risk of overfitting. To cover this broad frequency range with minimal peak amplitude, a total of 9 harmonics is selected, with $M = 9$.

Both damped Schroeder-phased harmonic (DS) and undamped Schroeder-phased harmonic (US) signals are used to model the wing displacement, whether it be pitch $\theta(t)$ or plunge $\xi(t)$. The US signal uniformly distributes energy across the frequency spectrum and is defined as:

$$\theta_{US}(t) = \sum_{m=1}^M a_m \sin((m+1)\omega_m t + \phi_m) \quad (\text{A.1})$$

where a_m represents the amplitude of the m -th component, ω_m denotes the angular frequency, and ϕ_m corresponds to the phase of the m -th sinusoidal component.

For transient response analysis, the DS signal simulates amplitude decay over time, incorporating a damping function:

$$\theta_{DS}(t) = \sum_{m=1}^M \left(\left(\frac{a_{\text{end}} - a_0}{t_{\text{end}} - t_0} (t - t_0) + a_0 \right) \sin((m+1)\omega_m t + \phi_m) \right) \quad (\text{A.2})$$

where a_0 and a_{end} denote the initial and final amplitudes, respectively, and t_0 and t_{end} are the corresponding time intervals. The damping is designed such that at the final time step, the amplitude is reduced to $0.1 a_0$, ensuring transient behaviors are effectively captured.

The phases ϕ_m are calculated to minimize constructive interference between the sinusoidal components, flattening the overall spectrum:

$$\phi_m = -\frac{m(m+1)\pi}{M} \quad (\text{A.3})$$

Appendix B. Models Architecture

This section outlines the architecture and training process for both the ARMAX and feedforward models used in this study, as detailed in Tables B.7 and B.8. The ARMAX model in Table B.7 combines autoregressive components with GCN layers and STGCN temporal layer to capture both spatial and temporal dynamics, featuring 5,775,023 trainable weights. In contrast, the feedforward model in Table B.8 avoids using previous predictions, which helps prevent error accumulation over time. This model has 1,962,111 trainable weights. Both models utilize a pre-trained AE for dimensionality reduction. Specifically, the Encoding A and Decoding layers in both architectures are optimized based on the pre-trained AE, while Encoding B mirrors the structure of Encoding A, ensuring consistent feature extraction across different model variants. Additionally, the concatenation block in both models concatenates the encodings from the previous three timesteps, enabling the temporal layer to effectively capture and process the sequential dependencies within the data.

During the backpropagation phase, the ADaptive Moment Estimation (Adam) optimizer [47] was employed to fine-tune the neural network weights and minimize

the MAE loss function. The learning rate was set to 0.001. A batch size m of 1 was found to yield the most accurate results. The training process was carried out over 50 epochs.

Encoding A	Layer Type	Output Size	Encoding B	Layer Type	Output Size
	Input	$m \times 3 \times 86840 \times 8$		Input	$m \times 3 \times 86840 \times 1$
	GCN	$m \times 3 \times 86840 \times 256$		GCN	$m \times 3 \times 86840 \times 256$
	GCN	$m \times 3 \times 86840 \times 224$		GCN	$m \times 3 \times 86840 \times 224$
	GCN	$m \times 3 \times 86840 \times 96$		GCN	$m \times 3 \times 86840 \times 96$
	Pooling 1	$m \times 3 \times 28600 \times 96$		Pooling 1	$m \times 3 \times 28600 \times 96$
	GCN	$m \times 3 \times 28600 \times 64$		GCN	$m \times 3 \times 28600 \times 64$
	Pooling 2	$m \times 3 \times 9600 \times 64$		Pooling 2	$m \times 3 \times 9600 \times 64$
GCN	$m \times 3 \times 9600 \times 368$	GCN	$m \times 3 \times 9600 \times 368$		

Concatenate Block – Output: $m \times 3 \times 9600 \times 736$

Temporal Layer – Output: $m \times 9600 \times 368$

Decoding	Layer Type	Output Size
	GCN	$m \times 9600 \times 368$
	Unpooling 2	$m \times 28600 \times 368$
	GCN	$m \times 28600 \times 64$
	Unpooling 1	$m \times 86840 \times 64$
	GCN	$m \times 86840 \times 96$
	GCN	$m \times 86840 \times 224$
	GCN	$m \times 86840 \times 256$
	Output	$m \times 86840 \times 1$

Table B.7: Layer structure and output dimensions for the ARMAX model, detailing the two encodings, temporal, and decoding layers used for predicting pressure distribution.

References

- [1] J. D. Anderson, J. Wendt, Computational fluid dynamics, volume 206, Springer, 1995.
- [2] J. Blazek, Computational fluid dynamics: principles and applications, Butterworth-Heinemann, 2015. doi:10.1016/C2013-0-19038-1.
- [3] C. Sabater, P. Stürmer, P. Bekemeyer, Fast predictions of aircraft aerodynamics using deep-learning techniques, AIAA Journal 60 (2022) 5249–5261. doi:10.2514/1.J061234.

Encoding A	Layer Type	Output Size
	Input	$m \times 3 \times 86840 \times 8$
	GCN	$m \times 3 \times 86840 \times 256$
	GCN	$m \times 3 \times 86840 \times 224$
	GCN	$m \times 3 \times 86840 \times 96$
	Pooling 1	$m \times 3 \times 28600 \times 96$
	GCN	$m \times 3 \times 28600 \times 64$
	Pooling 2	$m \times 3 \times 9600 \times 64$
	GCN	$m \times 3 \times 9600 \times 368$
Temporal Layer – Output: $m \times 9600 \times 368$		
Decoding	Layer Type	Output Size
	GCN	$m \times 9600 \times 368$
	Unpooling 2	$m \times 28600 \times 368$
	GCN	$m \times 28600 \times 64$
	Unpooling 1	$m \times 86840 \times 64$
	GCN	$m \times 86840 \times 96$
	GCN	$m \times 86840 \times 224$
	GCN	$m \times 86840 \times 256$
	Output	$m \times 86840 \times 1$

Table B.8: Layer structure and output dimensions for the Feedforward model, detailing the encoding, temporal, and decoding layers used for predicting pressure distribution.

- [4] R. Castellanos, J. B. Varela, A. Gorgues, E. Andrés, An assessment of reduced-order and machine learning models for steady transonic flow prediction on wings, in: ICAS 2022, 2022.
- [5] G. Immordino, A. Da Ronch, M. Righi, Steady-state transonic flowfield prediction via deep-learning framework, AIAA Journal (2024) 1–17. doi:10.2514/1.J063545.
- [6] J. Tompson, K. Schlachter, P. Sprechmann, K. Perlin, Accelerating eulerian fluid simulation with convolutional networks, in: International conference on machine learning, PMLR, 2017, pp. 3424–3433. doi:10.48550/arXiv.1607.03597.
- [7] M. M. Bronstein, J. Bruna, Y. LeCun, A. Szlam, P. Vandergheynst, Geometric deep learning: going beyond euclidean data, IEEE Signal Processing Magazine 34 (2017) 18–42. doi:10.1109/MSP.2017.2693418.
- [8] M. Gori, G. Monfardini, F. Scarselli, A new model for learning in graph domains,

in: Proceedings. 2005 IEEE International Joint Conference on Neural Networks, 2005., volume 2, IEEE, 2005, pp. 729–734. doi:10.1109/IJCNN.2005.1555942.

- [9] F. Scarselli, M. Gori, A. C. Tsoi, M. Hagenbuchner, G. Monfardini, The graph neural network model, *IEEE transactions on neural networks* 20 (2008) 61–80. doi:10.1109/TNN.2008.2005605.
- [10] Z. Wu, S. Pan, F. Chen, G. Long, C. Zhang, S. Y. Philip, A comprehensive survey on graph neural networks, *IEEE transactions on neural networks and learning systems* 32 (2020) 4–24. doi:10.1109/TNNLS.2020.2978386.
- [11] Z. Zhang, P. Cui, W. Zhu, Deep learning on graphs: A survey, *IEEE Transactions on Knowledge and Data Engineering* 34 (2020) 249–270. doi:10.1109/TKDE.2020.2981333.
- [12] J. Zhou, G. Cui, S. Hu, Z. Zhang, C. Yang, Z. Liu, L. Wang, C. Li, M. Sun, Graph neural networks: A review of methods and applications, *AI open* 1 (2020) 57–81. doi:10.1016/j.aiopen.2021.01.001.
- [13] T. N. Kipf, M. Welling, Semi-supervised classification with graph convolutional networks, *arXiv preprint arXiv:1609.02907* (2016). doi:10.48550/arXiv.1609.02907.
- [14] X. Jin, P. Cheng, W.-L. Chen, H. Li, Prediction model of velocity field around circular cylinder over various reynolds numbers by fusion convolutional neural networks based on pressure on the cylinder, *Physics of Fluids* 30 (2018) 047105. doi:10.1063/1.5024595.
- [15] K. Fukami, K. Fukagata, K. Taira, Super-resolution reconstruction of turbulent flows with machine learning, *Journal of Fluid Mechanics* 870 (2019) 106–120. doi:10.1017/jfm.2019.238.
- [16] N. Omata, S. Shirayama, A novel method of low-dimensional representation for temporal behavior of flow fields using deep autoencoder, *Aip Advances* 9 (2019) 015006. doi:10.1063/1.5067313.
- [17] J.-Z. Peng, S. Chen, N. Aubry, Z.-H. Chen, W.-T. Wu, Time-variant prediction of flow over an airfoil using deep neural network, *Physics of Fluids* 32 (2020) 123602. doi:10.1063/5.0022222.

- [18] V. Rozov, C. Breitsamter, Data-driven prediction of unsteady pressure distributions based on deep learning, *Journal of Fluids and Structures* 104 (2021) 103316. doi:10.1016/j.jfluidstructs.2021.103316.
- [19] R. Han, Y. Wang, Y. Zhang, G. Chen, A novel spatial-temporal prediction method for unsteady wake flows based on hybrid deep neural network, *Physics of Fluids* 31 (2019). doi:10.1063/1.5127247.
- [20] E. Saetta, R. Tognaccini, G. Iaccarino, Machine learning to predict aerodynamic stall, *International Journal of Computational Fluid Dynamics* 36 (2022) 641–654. doi:10.1080/10618562.2023.2171021.
- [21] D. Masegur Sampietro, A. Da Ronch, Graph convolutional multi-mesh autoencoder for steady transonic aircraft aerodynamics, *Machine Learning: Science and Technology* (2023). doi:10.1088/2632-2153/ad36ad.
- [22] G. E. Hinton, R. R. Salakhutdinov, Reducing the dimensionality of data with neural networks, *science* 313 (2006) 504–507. doi:10.1126/science.1127647.
- [23] P. Vincent, H. Larochelle, Y. Bengio, P.-A. Manzagol, Extracting and composing robust features with denoising autoencoders, in: *Proceedings of the 25th international conference on Machine learning*, 2008, pp. 1096–1103. doi:10.1145/1390156.1390294.
- [24] G. Immordino, A. Vaiuso, A. Da Ronch, M. Righi, Predicting transonic flowfields in non-homogeneous unstructured grids using autoencoder graph convolutional networks, *arXiv preprint arXiv:2405.04396* (2024). doi:10.48550/arXiv.2405.04396.
- [25] S. Hochreiter, J. Schmidhuber, Long short-term memory, *Neural computation* 9 (1997) 1735–1780. doi:10.1162/neco.1997.9.8.1735.
- [26] K. Cho, B. Van Merriënboer, D. Bahdanau, Y. Bengio, On the properties of neural machine translation: Encoder-decoder approaches, *arXiv preprint arXiv:1409.1259* (2014). doi:10.3115/v1/W14-4012.
- [27] H. Salehinejad, S. Sankar, J. Barfett, E. Colak, S. Valaee, Recent advances in recurrent neural networks, *arXiv preprint arXiv:1801.01078* (2017). doi:10.48550/arXiv.1801.01078.

- [28] K. Li, J. Kou, W. Zhang, Deep neural network for unsteady aerodynamic and aeroelastic modeling across multiple mach numbers, *Nonlinear Dynamics* 96 (2019) 2157–2177. doi:10.1007/s11071-019-04915-9.
- [29] S. L. Brunton, B. R. Noack, P. Koumoutsakos, Machine learning for fluid mechanics, *Annual review of fluid mechanics* 52 (2020) 477–508. doi:10.1146/annurev-fluid-010719-060214.
- [30] Q. Wang, C. E. Cesnik, K. Fidkowski, Multivariate recurrent neural network models for scalar and distribution predictions in unsteady aerodynamics, in: *AIAA Scitech 2020 Forum*, 2020, p. 1533. doi:10.2514/6.2020-1533.
- [31] A. Mannarino, P. Mantegazza, Nonlinear aeroelastic reduced order modeling by recurrent neural networks, *Journal of Fluids and Structures* 48 (2014) 103–121. doi:10.1016/j.jfluidstructs.2014.02.016.
- [32] A. Vaswani, N. Shazeer, N. Parmar, J. Uszkoreit, L. Jones, A. N. Gomez, L. Kaiser, I. Polosukhin, Attention is all you need, *Advances in neural information processing systems* 30 (2017). doi:10.48550/arXiv.1706.03762.
- [33] J. Cheng, L. Dong, M. Lapata, Long short-term memory-networks for machine reading, *arXiv preprint arXiv:1601.06733* (2016). doi:10.18653/v1/D16-1053.
- [34] X. Cheng, F. Shi, M. Zhao, G. Li, H. Zhang, S. Chen, Temporal attention convolutional neural network for estimation of icing probability on wind turbine blades, *IEEE Transactions on Industrial Electronics* 69 (2021) 6371–6380. doi:10.1109/TIE.2021.3090702.
- [35] X. Han, H. Gao, T. Pfaff, J.-X. Wang, L.-P. Liu, Predicting physics in mesh-reduced space with temporal attention, *arXiv preprint arXiv:2201.09113* (2022). doi:10.48550/arXiv.2201.09113.
- [36] J. Du, X. Li, S. Dong, Z. Liu, G. Chen, A novel attention enhanced deep neural network for hypersonic spatiotemporal turbulence prediction, *Physics of Fluids* 36 (2024). doi:10.1063/5.0210966.
- [37] J. Bai, J. Zhu, Y. Song, L. Zhao, Z. Hou, R. Du, H. Li, A3t-gcn: Attention temporal graph convolutional network for traffic forecasting, *ISPRS International Journal of Geo-Information* 10 (2021) 485. doi:10.48550/arXiv.2006.11583.

- [38] D. K. Duvenaud, D. Maclaurin, J. Iparraguirre, R. Bombarell, T. Hirzel, A. Aspuru-Guzik, R. P. Adams, Convolutional networks on graphs for learning molecular fingerprints, *Advances in neural information processing systems* 28 (2015). doi:10.48550/arXiv.1509.09292.
- [39] M. Fey, J. E. Lenssen, Fast graph representation learning with pytorch geometric, 2019. doi:10.48550/arXiv.1903.02428. arXiv:1903.02428.
- [40] D. K. Hammond, P. Vandergheynst, R. Gribonval, Wavelets on graphs via spectral graph theory, *Applied and Computational Harmonic Analysis* 30 (2011) 129–150. doi:10.1016/j.acha.2010.04.005.
- [41] X. SHI, Z. Chen, H. Wang, D.-Y. Yeung, W.-k. Wong, W.-c. WOO, Convolutional lstm network: A machine learning approach for precipitation nowcasting, in: C. Cortes, N. Lawrence, D. Lee, M. Sugiyama, R. Garnett (Eds.), *Advances in Neural Information Processing Systems*, volume 28, Curran Associates, Inc., 2015. doi:10.48550/arXiv.1506.04214.
- [42] Y. Seo, M. Defferrard, P. Vandergheynst, X. Bresson, Structured sequence modeling with graph convolutional recurrent networks, in: *Neural Information Processing: 25th International Conference, ICONIP 2018, Siem Reap, Cambodia, December 13-16, 2018, Proceedings, Part I 25*, Springer, 2018, pp. 362–373. doi:10.48550/arXiv.1612.07659.
- [43] B. Yu, H. Yin, Z. Zhu, Spatio-temporal graph convolutional networks: A deep learning framework for traffic forecasting, arXiv preprint arXiv:1709.04875 (2017). doi:10.24963/ijcai.2018/505.
- [44] R. De Maesschalck, D. Jouan-Rimbaud, D. L. Massart, The mahalanobis distance, *Chemometrics and intelligent laboratory systems* 50 (2000) 1–18. doi:10.1016/j.patcog.2008.05.018.
- [45] J. Heeg, Overview of the aeroelastic prediction workshop, in: *51st AIAA aerospace sciences meeting including the new horizons forum and aerospace exposition, 2013*, p. 783. doi:10.2514/6.2013-783.
- [46] T. D. Economon, F. Palacios, S. R. Copeland, T. W. Lukaczyk, J. J. Alonso, Su2: An open-source suite for multiphysics simulation and design, *Aiaa Journal* 54 (2016) 828–846. doi:10.2514/1.J053813.
- [47] D. P. Kingma, J. Ba, Adam: A method for stochastic optimization, arXiv preprint arXiv:1412.6980 (2014). doi:10.48550/arXiv.1412.6980.